JOURNAL OF PETROLOGY

Journal of Petrology, 2022, Vol. 63, No. 3, 1–28
https://doi.org/10.1093/petrology/egac008
Advance Access Publication Date: 14 February 2022
Original Manuscript

OXFORD

The Palaeoproterozoic Gallujavri Ultramafic Intrusion, Karasjok Greenstone Belt; Petrogenesis of a Trans-Crustal Magma System

Alf Andre Orvik[1,*], Trond Slagstad[2], Harald Hansen[3], Lars Petter Nilsson[2], and Bjørn Eske Sørensen[1]

[1]Department of Geoscience and Petroleum, Norwegian University of Science and Technology, S. P. Andersens veg 15, 7031 Trondheim, Norway [2]Geological Survey of Norway, Leiv Eirikssons vei 39, 7040 Trondheim, Norway and [3]Department of Geosciences, UiT The Arctic University of Norway, Dramsveien 201, 9037 Tromsø, Norway

*Corresponding author. Telephone: +47 93 444 158. E-mail: alf.a.orvik@ntnu.no

Received 16 August 2021; Revised 20 December 2021; Accepted 11 February 2022

Abstract

The modern concepts of magmatic plumbing systems have evolved from simple models of melt-dominated crustal magma chambers to magmatic systems that span the continental crust. The geochemistry of these systems is challenging to model numerically because of a complex polybaric and multiphase evolution, which is not well described by mathematic end-member formulas. We propose that a recent modelling tool, the Magma Chamber Simulator (MCS), can reveal part of the petrological complexities of such systems. The MCS numerically models phase equilibria, mineral chemistry and major and trace elements in multicomponent–multiphase systems by finding the extremes of the appropriate state functions. This study presents new petrographical and geochemical data from the Palaeoproterozoic Gallujavri ultramafic intrusion in the Karasjok Greenstone Belt, Arctic Norway. Our data indicate that (1) the intrusion is affected by crustal assimilation, (2) phase equilibria require polybaric crystallisation and (3) spinel compositions are similar to sub-volcanic intrusions of continental flood basalt provinces. We utilise the MCS to simulate the petrogenesis of the intrusion and test the model by comparing it against our reported petrological and geochemical data. Our modelling shows that the parental magma of the intrusion is consistent with coeval Karasjok-type komatiites observed at various places throughout the greenstone belt. First, the komatiitic primary magma intruded Archaean lower crust (c. 700 MPa), where fractionation and assimilation resulted in a hybrid melt. Second, the hybrid melt migrated and accumulated in a mid-crustal magma chamber (c. 400 MPa), where it continued to fractionate and assimilate while remaining open to recharge of mantle-derived komatiitic melts, forming the Gallujavri intrusion. We interpret the Gallujavri intrusion as part of a Palaeoproterozoic trans-crustal magma plumbing system, with many similarities to other Fennoscandian ultramafic-mafic layered intrusions.

Key words: magma plumbing systems; magma evolution; Magma Chamber Simulator; Karasjok Greenstone Belt; Gallujavri intrusion

INTRODUCTION

Interaction between Earth's crust and mantle-derived melts passing through or ponding at its base is key in controlling the chemical evolution of such melts (Ganne *et al.*, 2018). Classically, the observed petrological diversity of igneous rocks is attributed to mechanisms of melt generation, differentiation and assimilation *en route* to the surface. Of critical importance to igneous petrology is deciphering the melt storage location(s) and the routes taken towards the surface (Magee *et al.*, 2018). In the past two decades, innovations in geophysical methods have allowed imaging of zones of melt accumulation and magma migration (Magee *et al.*, 2018, and references therein). Together with accumulating evidence from geochemical, petrological, volcanological and geological observations, these data fuel an

emerging consensus that melts are stored and transported in complex and vertically extensive magmatic systems (e.g. Annen *et al*., 2006; Blundy *et al*., 2008; Cashman *et al*., 2017; Hildreth & Moorbath, 1988; Sinton & Detrick, 1992; ; Tarasewicz *et al*., 2012). In light of this knowledge, a major obstacle to geochemical modelling is that the complex and polybaric nature of the system causes chemical variations that are not easily described by classical mathematical descriptions of melt differentiation and assimilation (Cashman *et al*., 2017). However, a recently developed tool, the Magma Chamber Simulator (MCS), quantifies concurrent recharge, assimilation and crystallisation via mass and enthalpy balance in multicomponent and polyphase systems (Bohrson *et al*., 2014), thus representing a significant step forward in overcoming these issues.

In this contribution, we report petrographic and geochemical data from the Palaeoproterozoic Gallujavri ultramafic intrusion in Arctic Norway. The intrusion is part of the Karasjok and Central Lapland Greenstone Belt (KCLGB), extending from Norway, through Finland, into Russia, containing several types of (ultra)mafic plutonic bodies and coeval extrusive rocks (Fig. 1). The MCS tool allows us to model the petrological evolution of the Gallujavri intrusion and compare the model results against our reported petrological and geochemical data. The model reveals that magma transport via a two-stage polybaric plumbing system can be used to explain several of the phase equilibria and major and trace element characteristics of the Gallujavri intrusion. Our findings are consistent with recent models of transcrustal magma systems developed from active conduits (Farrell *et al*., 2014; Huang *et al*., 2015; Magee *et al*., 2018) and show that these concepts can likely be extended to Palaeoproterozoic magmatism in Fennoscandia.

REGIONAL GEOLOGY

The Karasjok Greenstone Belt (KGB) lies in the northwestern portion of the Fennoscandian Shield (Fig. 1) and, along with the Kautokeino Greenstone Belt, constitutes the northernmost part of a nearly 100-km-wide Palaeoproterozoic tectonic belt that extends from northwestern Russia, through northern Finland, into northern Norway (Braathen & Davidsen, 2000).

The KGB has a north–south trend and is ~160 km long and between 20 and 40 km wide (Krill, 1985b; Barnes & Often, 1990) and continues into Finland, where it is named the Central Lapland Greenstone Belt, which gives a total length of ~310 km (Barnes & Often, 1990).

The KGB lithostratigraphy comprises supracrustal and intrusive rocks metamorphosed to medium grade (Fig. 2; Braathen & Davidsen, 2000). To the west, the KGB nonconformably overlies and is partly thrust over the tonalite–trondhjemite–granodiorite (TTG)-dominated Archaean Jergul Gneiss Complex (Fig. 2a; Bingen *et al*., 2015, Hansen *et al*., 2020). It is bounded to the east by the overthrust Tanaelv Migmatite Complex (Siedlecka, 1985; Braathen & Davidsen, 2000). To the north, the belt is overlain by sedimentary rocks and allochthonous Caledonian nappes.

The lowest unit in the KGB stratigraphy is the Lavttevàrri formation (Fig. 2b). This 50–150-m-thick formation consists mainly of fine-grained foliated amphibolites, metapelites and metakomatiites. Rocks above the basal unconformity include mica schists with carbonates and locally conglomerates consisting of granite and granitic gneisses from the basement (Braathen & Davidsen, 2000).

The Čorgaš formation (Fig. 2c) is 250–700 m thick with a lower portion comprising conglomerates, psammites and metapelites and an upper section consisting of shallow-marine sedimentary rocks and subaerial to shallow-water mafic volcanic rocks (Barnes & Often, 1990; Braathen & Davidsen, 2000; Stokmo, 2020). Carbon isotope chemostratigraphy on carbonates within the formation indicates a depositional age between 2220 and 2140 Ma (Melezhik *et al*., 2015). The isotope chemostratigraphy provides a likely maximum age of the ultramafic and mafic intrusions that are common in this formation, including the Gallujavri intrusion, which is the topic of this contribution. Considering that the (ultra)mafic layered intrusions of the KCLGB are interpreted to have formed in discrete magmatic episodes at 2440, 2220 and 2050 Ma (Hanski & Huhma, 2005), the intrusions within the Čorgaš formation, including Gallujavri, is likely part of the last pulse. Previous studies have also highlighted many lithological similarities between the Gallujavri intrusion and the c. 2.06 Ga Kevitsa intrusion in Finland (Nilsson & Often, 2009), further corroborated by recent unpublished U–Pb geochronological data (Orvik *et al*., in preparation).

Tholeiitic basalts represented by banded amphibolites dominate the 300 to 700 m-thick Briittágielas formation (Fig. 2d). The lower part of the formation includes calc-alkaline dacitic metavolcanic rocks and kyanite-bearing garnet-mica schists. The basal contact towards the underlying Čorgaš formation is marked by an extensive marble unit (Braathen & Davidsen, 2000). The Briittágielas formation is also distinguished by four 70-m-thick units of metakomatiite (Barnes & Often, 1990; Braathen & Davidsen, 2000).

The Fossestrand formation (Fig. 2e) appears in the core of a regional-scale isoclinal fold with an across-strike thickness of 250–300 m (Stokmo, 2020). Metakomatiitic and volcanoclastic rocks dominate the formation. The lower section consists of two thick pillowed lava flows, while the upper portion consists of lava flows and agglomerates. Coarser-grained mafic rocks have also been identified within this formation (Braathen & Davidsen, 2000).

Palaeoproterozoic komatiites and picrites occur at various stratigraphic levels in the KCLGB (Fig. 1; Barnes & Often, 1990, Hanski & Huhma, 2005, Puchtel *et al*., 2020) and consist of both Munro-type komatiites, Karasjok-type (Ti-enriched) komatiites and ferropicritic compositions (Barnes & Often, 1990; Puchtel *et al*., 1997; Hanski *et al*., 2001a; Heggie *et al*., 2013). In Finland, the Palaeoproterozoic ultramafic volcanic rocks extruded on the fine-grained metasedimentary rocks of the Savukoski group and consist of Karasjok-type komatiites and picrites (Barnes & Often, 1990; Hanski *et al*., 2001a; Heggie *et al*., 2013). The Savukoski group has a minimum age of deposition provided by cross-cutting intrusive bodies, such as the 2058 ± 4 Ma Kevitsa layered intrusion (Mutanen & Huhma, 2001).

Recently, Puchtel *et al*. (2020) determined a Re–Os isochron age of 2049 ± 13 Ma for komatiite whole-rock and olivine and chromite separates from the Kevitsa and Jeesiorova area. Pyroxene and whole-rock Sm–Nd pairs yielded an isochron age of 2046 ± 22 Ma. These ages are comparable to the Sm–Nd isochron age for the Jeesiorova and Kittila komatiites (2056 ± 25 Ma; Hanski *et al*., 2001a) and komatiites of the KGB (2085 ± 85 Ma; Krill, 1985a). Puchtel *et al*. (1998) noted that the age determinations from the Karasjok komatiites use whole-rock Sm–Nd on geochemically heterogeneous samples, cautioning the significance of this age. However, the komatiites in different parts of the belt can still be correlated based on similar stratigraphic position, lithology and geochemistry (Puchtel *et al*., 1997; Hanski *et al*., 2001a; Heggie *et al*., 2013), implying vast and contemporaneous outpourings of mafic–ultramafic magmas over much of the Fennoscandian Shield (Puchtel *et al*., 1998).

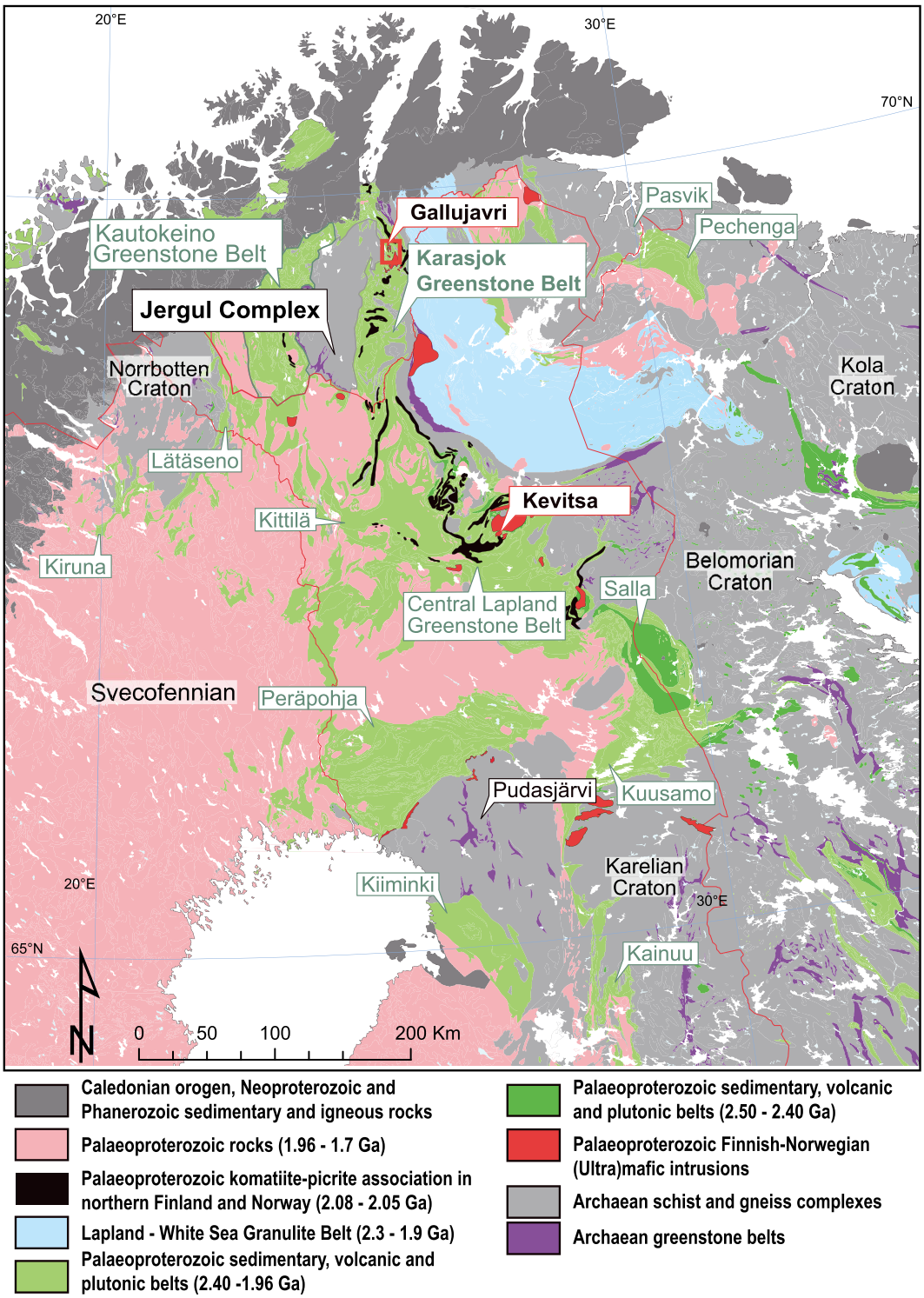

Fig. 1. Simplified map of northern Fennoscandia, modified from Bingen *et al*. (2015), Hanski *et al*. (2001a), Hanski & Huhma (2005), and Puchtel *et al*. (2020), based on Koistinen *et al*. (2001). Red bodies mark layered ultramafic-mafic intrusions and anorthosite, and black bodies mark occurrences of the Palaeoproterozoic komatiite–picrite association of Norway and northern Finland. The red box shows the location of Fig. 3 and the location of the ultramafic Gallujavri intrusion.

THE GALLUJAVRI ULTRAMAFIC INTRUSION

The Gallujavri intrusion is a small sill-like ultramafic body covering a surface area of c. 2.3 km^2 (Fig. 3). As for the rest of the KGB, exposure is limited and the intrusion shows a clear eastward continuation on geophysical maps (Fig. 3b,c; Skaar, 2014), suggesting it is larger than implied by the surface expression.

The intrusion is hosted by the 45–70° eastward-dipping quartzitic and quartz-feldspathic schists of the Corgaš Formation (Nilsson & Often, 2009, and references therein). The metasedimentary rocks are

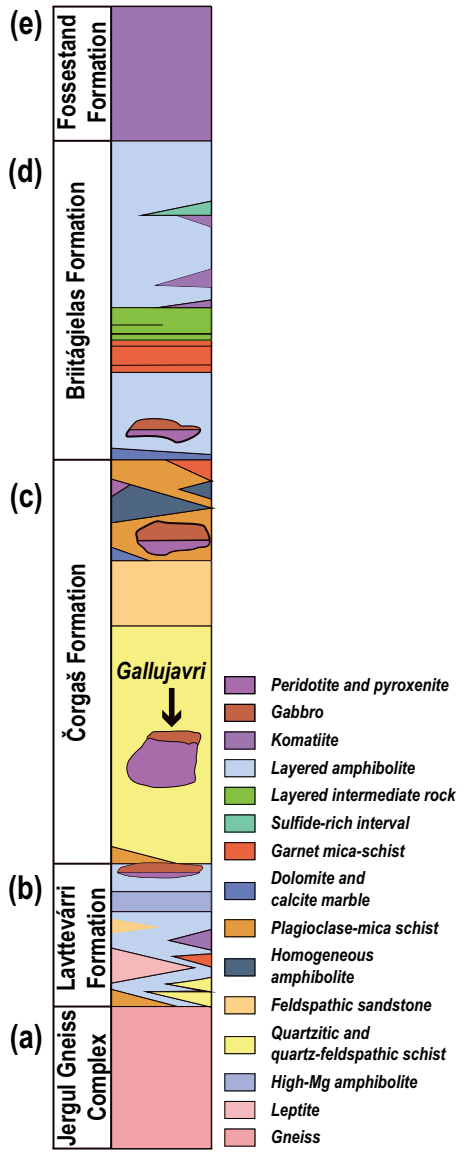

Fig. 2. The lithostratigraphy of the Karasjok Greenstone belt, modified from Hansen *et al.* (2020).

fine grained, light grey with a quartz and feldspar content of c. 80%, followed by micas, amphibole and accessory garnet (Bradley, 2003). The eastern contact of the intrusion consists of a variably altered olivine pyroxenite that grades to gabbro with c. 30% intercumulus plagioclase. Despite the alteration, primary features are locally preserved, including pristine magmatic mineralogy. The intrusion hosts mineralisations of disseminated sulphide consisting of up to 5% interstitial and intergrown chalcopyrite, pyrrhotite and pentlandite. The mineralisations are found in the ultramafic parts and gabbros but are also associated with alteration, faulting and contact zones (Bradley, 2003).

SAMPLING, ANALYTICAL AND MODELLING METHODS

Eleven holes have been drilled—eight pack-sack holes and three diamond drill holes (03GD001–003; Fig. 3) —together with geophysics, geological mapping and geochemical sampling (Boyd *et al.*, 2016). The sampling and analytical procedures reflect the exploratory nature of prior studies. Therefore, the three diamond drill cores were relogged, sampled and analysed. From the three cores, we extracted 66 samples, from which 60 samples were sent for geochemical analysis and 59 polished thin sections were made.

Major and trace element abundances

The sixty whole-rock samples from the three re-analysed drill holes were analysed at the ALS laboratories in Piteå, Sweden (Supplement 1). Major, minor and trace elements were analysed with fused bead, acid digestion using inductively coupled plasma atomic-emission spectroscopy (ICP–AES) and inductively coupled plasma mass spectrometry (ICP–MS). Base metals were analysed by ICP–AES following four-acid digestion.

Analysis of mineral compositions

Electron probe micro-analysis

Electron probe micro-analysis (EPMA) analyses were conducted on eight thin sections at the Norwegian University of Science and Technology (NTNU), Trondheim, using a JEOL JXF–8530F PLUS field-emission (FE) microprobe, set to 15 keV and 10 nA for all analyses. Counting times varied from 5 s on peak and 2 s on high and low background for Na in plagioclase to 50 s on peak and 25 s on each background for F in mica and amphibole. Most elements had counting times of 20 and 10 s on peak and backgrounds, respectively (Supplement 2). 4 wt% H_2O was added as matrix correction to the mica analyses and 2 wt% in the amphibole analyses. The mass-based model of Ridolfi *et al.* (2018) was later used to accommodate the volatile content in the amphiboles.

Laser-ablation inductively coupled plasma mass spectrometry

Minor and trace element concentrations in Fe–Ti oxides were analysed by laser-ablation inductively coupled plasma mass spectrometry (LA–ICP–MS; Supplement 3) using an ELEMENT XR at the Geological Survey of Norway, Trondheim. A total of 14 grains were analysed located in three thin sections.

The ELEMENT XR is a double-focusing sector-field inductively coupled plasma mass spectrometer linked to a New Wave UP193FX ESI excimer laser probe. The concentrations of trace elements were measured on polished thin sections (30 μm thickness). Iron concentrations determined by EPMA were used as the internal standard. The material used for external multi-standard calibration was the National Institute of Standards and Technology reference glasses NIST SRM 612 and NIST SRM 614 and the US Geological Survey references GSD–1G, GSE–1G, MASS–1 and BCR–2G.

Magma chamber simulator

The MCS is an energy and mass constrained thermodynamic tool for modelling magmatic evolution by fractional crystallisation (FC), assimilation and fractional crystallisation (AFC), recharge and fractional crystallisation (RFC) and recharge, assimilation and fractional crystallisation (RAFC) (Bohrson *et al.*, 2014). With this simulation tool, thermodynamic boundaries capable of transferring heat and mass separate the resident magma, recharge magma and wall-rock subsystems, for which the MCS calculates phase equilibria and geochemical evolution. The overall petrological and geochemical evolution is linked by the resident magma and wall-rock temperatures as the two advance towards thermal equilibrium. The resident magma

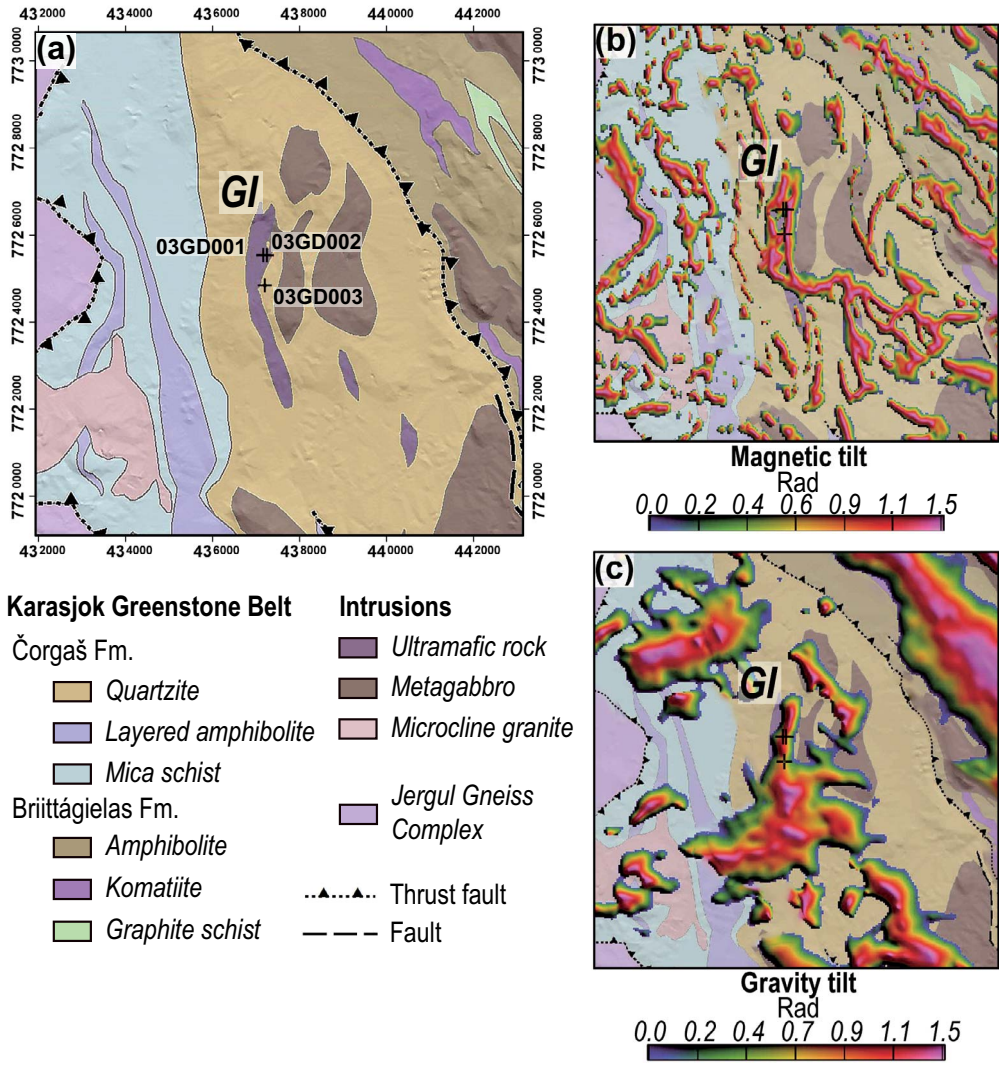

Fig. 3. Geological map and geophysical anomaly maps from Skaar (2014). All three maps cover the same area. The location of drill holes 03GD001, 03GD002 and 03GD003 are marked with crosses. (a) Geological map of the Gallujavri intrusion. (b) Magnetic tilt anomalies and (c) gravity tilt anomalies superimposed on the geological map. Gl, Gallujavri intrusion.

(with possible recharges) transfers enthalpy to the host rock so that the latter (potentially) exceeds its solidus temperature and thereby contaminates the initial melt. Assimilation of anatectic melts occurs only after exceeding a pre-determined critical melt-volume fraction defined as the percolation threshold (FmZero). The wall-rock and magma subsystems evolve due to mass and heat exchange, calculated at pre-determined temperature decrements with a selected MELTS engine (pMELTS or rhyolite-MELTS versions 1.0.x, 1.1.x, or 1.2.x; Ghiorso & Gualda, 2015, Ghiorso *et al*., 2002, Ghiorso & Sack, 1995, Gualda *et al*., 2012).

Definitions of subsystems and initial conditions

Only a brief outline of the MCS modelling parameters and boundary conditions is given here. For more information on these topics, we refer to several articles introducing MCS (e.g. Bohrson *et al*., 2014; Heinonen *et al*., 2019; Bohrson *et al*., 2020; Heinonen *et al*., 2020; Heinonen *et al*., 2021).

The progress variable of the MCS is magma temperature (**ΔT**), and each simulation is isobaric. Oxygen fugacity can be constrained to a specified redox buffer (e.g. QFM), providing a fixed f_{O2} as a function of temperature. Otherwise, the initial FeO and Fe_2O_3 concentrations can be specified for each subsystem.

The initial resident-magma subsystem (**M**) has specified bulk composition ($X^M_{0,i}$), where i refers to the ith chemical component and mass (M^M_0). The initial magma is completely molten at the time of intrusion, as the magma (T^M_0) temperature must be initialised at the liquidus temperature.

The next subsystem is the cumulates (**C**; solids±volatiles) that are transferred adiabatically in incremental batches from **M** to **C**. The mass transferred from **M** to **C** is determined by the mass of solids±volatiles formed (if any) in the temperature step (**ΔT**). The solids±volatiles form in thermal and chemical equilibrium with **M**, but no further chemical interaction is allowed once transferred to **C**.

The wall-rock (**WR**) subsystem thermally interacts and supplies anatectic melt (i.e. if above the percolation threshold) to **M**. The

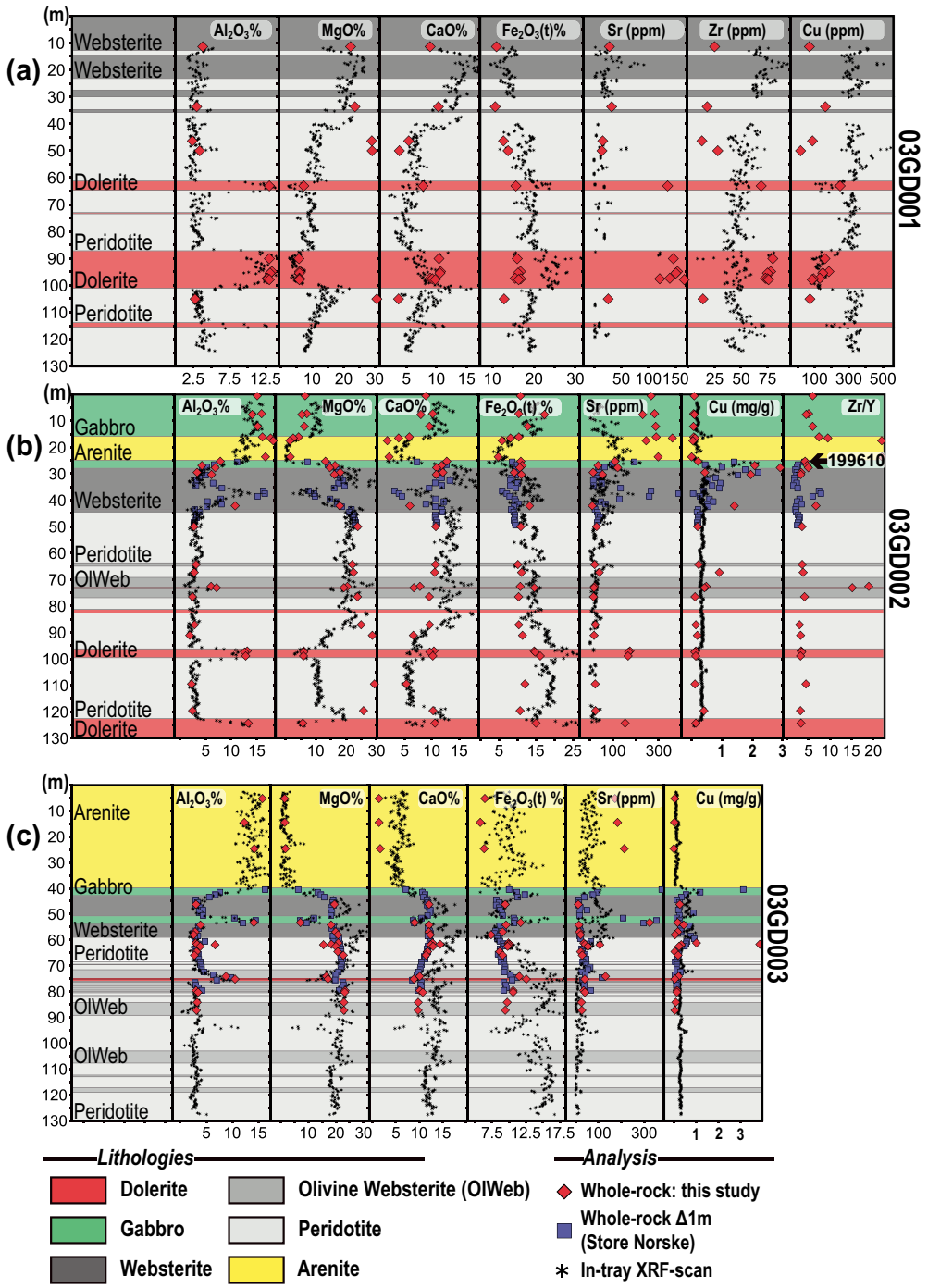

Fig. 4. Magmatic stratigraphy of drill holes logged and sampled in this study. The blue squares are whole-rock data determined by the commercial laboratory ALS for Store Norske. The red diamonds are whole-rock ICP–AES data from this study. The small black asterisks show semi-quantitative direct in-tray XRF scanning data acquired by Store Norske. We note that in some intervals, the XRF scans differ substantially from the other methods. (a) Drill hole 03GD001. (b) Drill hole 03GD002. Note the location of the CM sample 199 610. (c) Drill hole 03GD003.

wall rock (**WR**) is initialised with the specification of mass ($M^{WR}{}_0$), composition ($X^{WR}{}_{0,i}$) and initial temperature ($T^{WR}{}_0$) that is required to be below the solidus temperature. The $M^{WR}{}_0$ can be thought of as the proportion of wall rock capable of interacting with the resident magma.

Melt recharges ($\mathbf{R}_j$) can be added to **M** in j mass increments ($M^R{}_j$), each with a defined initial bulk composition ($X^R{}_{j,i}$) for i chemical components and temperature ($T^R{}_j$). Unlike **M**, the **R** magma temperature can be specified above or below the liquidus so that superheated melt or melt+crystals±volatiltes can be added to **M**. The specification of $T^R{}_j$ under the liquidus leads MCS to calculate the internal thermodynamic equilibrium (i.e. mineral modes and compositions) of the $\mathbf{R}_j$ subsystem before addition to **M**.

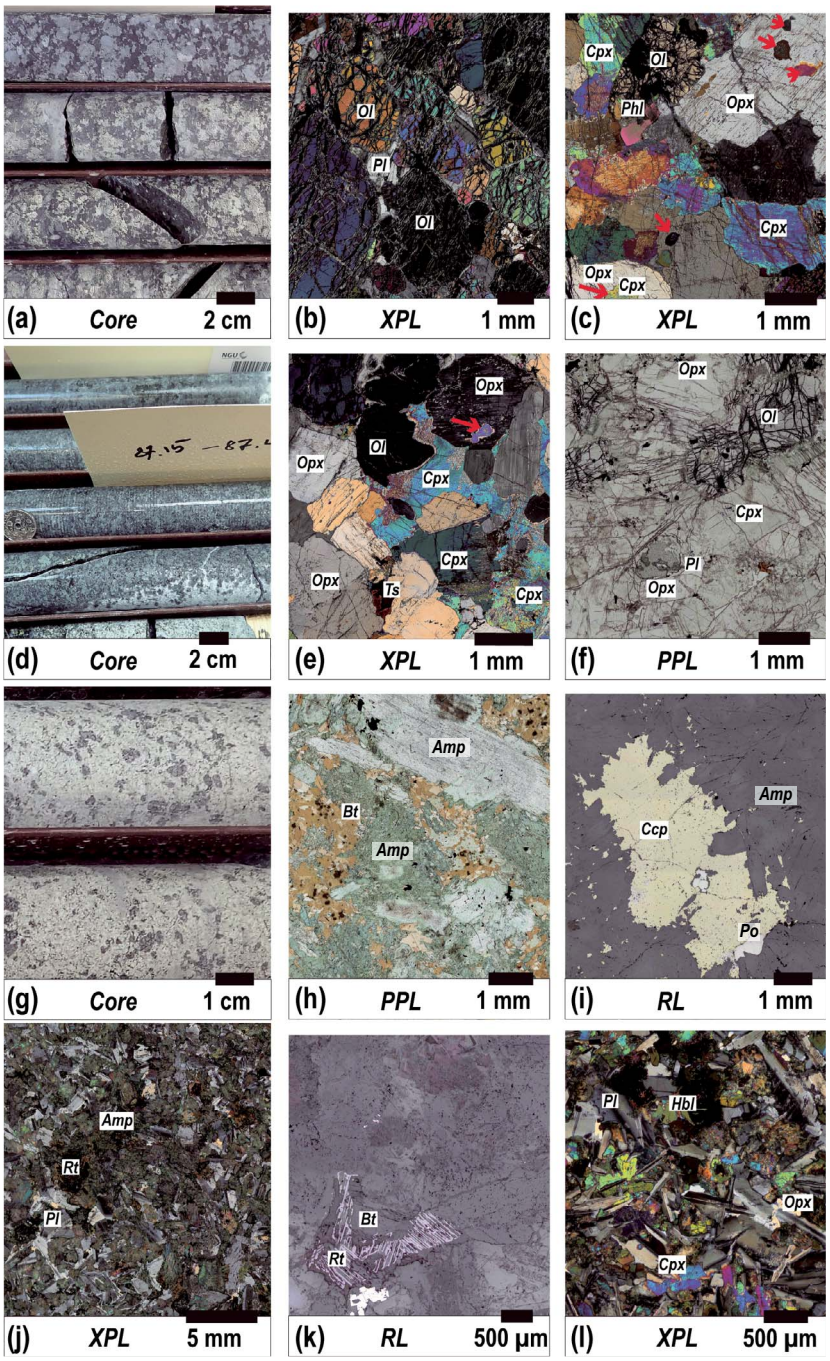

Fig. 5. Images and micrographs of common rocks of the Gallujavri ultramafic intrusion. (a) Image of a typical peridotite in drill core 03GD001. Serpentinisation and Fe-oxide alteration of primary olivine result in the black appearance in hand specimens. The white to light-green areas consist of orthopyroxene and clinopyroxene with tremolite, chlorite and serpentine alteration. (b) Micrograph showing a dunitic olivine adcumulate with interstitial plagioclase. (c) Micrograph showing a peridotite consisting of cumulate olivine and coarse-grained oikocrystic orthopyroxene. The clinopyroxene occurs as chadacrysts in orthopyroxene and as an anhedral interstitial phase. Red arrows point to examples of clinopyroxene inclusions in orthopyroxene. The intercumulus phases, together with clinopyroxene, consist of accessory phlogopite and plagioclase—the latter not visible in this image. (d) Image showing a typical olivine websteritic section in drill core 03GD003. (e) Micrograph showing an olivine, orthopyroxene and clinopyroxene mesocumulate with intercumulus clinopyroxene and hornblende. (f) Micrograph showing an olivine, clinopyroxene and oikocrystic orthopyroxene mesocumulate with intercumulus plagioclase. Clinopyroxene occurs as a cumulus phase and as chadacrysts in orthopyroxene. (g) Image of a typical websterite in drill core 03GD003. Pyroxenes and their alteration products are white to yellowish white; the dark phase is olivine. (h) Micrograph showing extensive amphibole–phlogopite alteration of a websteritic sample. Note the sizeable relict pyroxene in the upper right-hand corner replaced by amphibole. Also, note biotite with characteristic pleochroic haloes. (i) Micrograph of a large chalcopyrite grain in a groundmass of secondary amphibole. (j) Micrograph showing a coarse-grained intergranular gabbro. The spaces between the plagioclase crystals are occupied by heavily altered granules of pyroxenes and opaques. (k) Micrograph showing sagenitic-textured biotite in gabbro. (l) Micrograph showing intergranular dolerite, where the granules consist of pyroxenes and secondary Ca-amphibole. Abbreviations: cross-polarised light (XPL), plane-polarised light (PPL), reflected light (RL), plagioclase (Pl), clinopyroxene (Cpx), orthopyroxene (Opx), olivine (Ol), phlogopite (Phl), tchermakite (Ts), biotite (Bt), chalcopyrite (Ccp), pyrrhotite (Po), amphibole (Amp), rutile (Rt) and hornblende (Hbl).

RESULTS

Petrography

The three drill holes studied are oriented 45°/270° and consist of a lower section of peridotite, a middle section of pyroxenite and an upper section of gabbro (Fig. 4). The apparent internal lithological layering is perpendicular to the orientation of the drill holes, making the layering concordant or semi-concordant to the foliation of the surrounding metasedimentary rocks.

The lower part of the drilled section comprises lherzolitic to harzburgitic cumulates with variable intercumulus plagioclase (c. 0–3 modal%) and accessory hornblende and phlogopite (Fig. 5a–c). Primary olivine (50 to 80 modal%) has mesh textures consisting of serpentine and fine-grained oxides, making them black in hand specimen (Fig. 5a). In combination with accessory, primary dark-brown hornblende, there is moderate to severe amphibole alteration of clinopyroxene, whereas orthopyroxene (c. 20 modal%) generally shows more resistance to alteration. Orthopyroxene (c. 20 vol%) is generally coarse grained and unaltered and found in a ground-mass of serpentine, amphibole and chlorite.

Despite widespread alteration, many less-altered examples allow for the examination of primary igneous textures. These samples typically show considerable variation in the pyroxene-to-olivine ratio. Olivine is commonly anhedral and rounded with an average grain size of c. 2 mm. The second most abundant mineral is coarse-grained (c. 2–3 mm), commonly poikilitic orthopyroxene. Clinopyroxene (c. 0–20 modal%) occurs both as an anhedral interstitial phase and chadacrysts in olivine and orthopyroxene (Fig. 5c).

In drill holes 03GD002 and 03GD003 (Fig. 4b,c), the peridotite is interlayered with olivine websterite. These layers, however, cannot be correlated between the cores. The olivine websterite is composed primarily of cumulus orthopyroxene (5–45 modal%), clinopyroxene (6–52%) and olivine (4–20%), with interstitial plagioclase (0–5%), hornblende (0–4%) and phlogopite (0–3%) (Fig. 5d–f). Cumulus olivine and orthopyroxene both have average grain sizes of about 2 mm. Olivine is inequigranular, anhedral and rounded, while orthopyroxene generally is subhedral and equigranular. Clinopyroxene grains are less bounded by crystal faces and show greater variation in grain size than orthopyroxene. Clinopyroxene is commonly subordinate to orthopyroxene and seemingly crystallised at various melt-evolution stages, suggested by clinopyroxene appearing as cumulus grains, inclusions in orthopyroxene and as an intercumulus phase (Fig. 5e,f). Plagioclase occurs as a late interstitial phase (Fig. 5f).

The modal amounts of olivine in the peridotite and olivine websterite interlayers gradually decrease towards the top of the drill holes, becoming websteritic. The websterite is severely altered to a mineral association of green amphibole, tremolite, chlorite and mica, making most modal and textural evaluations of the primary mineralogy impossible (Fig. 5g–i). Some relicts of pyroxene indicate a coarse grain size of around 3.5 mm. Pleochroic haloes characterise secondary biotite (Fig. 5h). Examples of coarse-grained chalcopyrite (c. 6 mm) disseminations is found with minor pyrrhotite and pentlandite (Fig. 5i). In the top sections of drill holes 03GD002 and 03GD001 (Fig. 4a,b), the websterite grades into gabbro. The gabbro changes in texture and modal proportions from base to top. At the base, the gabbro is melanocratic with interstitial plagioclase (c. 20%) with an average grain size of c. 1 mm. The plagioclase is partly recrystallised, with rounded grain boundaries indicating post-magmatic reworking and grain-size reduction. The ferromagnesian minerals throughout this section are wholly recrystallised to green amphibole and chlorite. Pyrite, pentlandite, pyrrhotite and chalcopyrite are commonly present as fractionated products within millimetre-scale sulphide blebs.

Upsection, gabbros become coarser grained with almost unaltered cumulus plagioclase (Fig. 5j). The mafic minerals have suffered severe amphibole–biotite alteration—the biotite with rutile and titanite exsolution (Shau *et al.*, 1991)—giving them a beautiful and characteristic sagenitic texture (Fig. 5k). In drill hole 03GD002, a repetition of gabbro, separated by the arenitic host, represents the intrusion's chilled margin (CM; 25–28 m; cf. sample 199 610; Fig. 4b).

Throughout the magmatic stratigraphy, there are multiple examples of sheet intrusions of dolerite. These microgabbro dykes consist of plagioclase laths measuring ~500 μm along the c-axis with intergranular diopside, augite, olivine and orthopyroxene (Fig. 5l). The mafic minerals are moderate to severely altered, with green amphibole constituting 30 to 70%. At the mesoscale, these sheet intrusions have clear CMs. However, at the microscale, the fine-grained material is deformed and entirely replaced by alteration products.

Mineral chemistry

Below, we report our mineral chemical data acquired with EPMA (Table 1) and Fe–Ti oxide LA–ICP–MS (Table 2). Because of the large dataset, the ranges reported exclude outliers that are more than 1.5 times larger or smaller than the upper and lower quartiles, respectively. The complete dataset is available in Supplement 4.

Olivine from the different lithologies is homogeneous with no evidence of zoning (Fig. 6a, b). The olivine websterites have the most primitive forsterite content, with Fo_{80-82}. The plagioclase-bearing olivine websterite follows with Fo_{79-81}. The peridotites have forsterite contents spanning slightly lower values, with Fo_{78-79}, more reminiscent of olivine from a gabbroic host (Burns & Brown Jr., 1982). The forsterite content in the gabbro ranges from Fo_{76} to Fo_{77}. Depletion of CaO (<1000 ppm) is characteristic for olivine in all rock types except for the olivine websterite, which has elevated concentrations (>4500 ppm). The olivine has high Ni concentrations, with NiO in the range 2800–3500 ppm (Fig. 6b). Slightly lower values are seen in the gabbro, with NiO in the range 2700–2800 ppm.

The clinopyroxene of the intrusion is dominated by augite with a smaller amount of diopside (Fig. 6a). The peridotite hosts the most primitive clinopyroxene with xMg ($Mg/Mg+Fe^t$) in the narrow range 0.89–0.90. These samples also have the most Ca-poor clinopyroxenes with a CaO concentration of 12 ± 0.5%. The xMg of the clinopyroxene hosted by the olivine websterite ranges between 0.86 and 0.89, plagioclase-bearing olivine websterite between 0.81 and 0.86 and gabbro between 0.76 and 0.86 – all of them with CaO ranging from 17 to 22%. Most of the clinopyroxene has higher xMg relative to the olivine in a sample. The feature of $xMg_{Cpx} > Fo$ is typical for high-T peridotites. It indicates an equilibrium distribution of Fe and Mg between the two phases (Fig. 6c; Barsdell, 1988, Grant *et al.*, 2016, Jagoutz *et al.*, 2007, Perkins & Vielzeuf, 1992). The disequilibrium seen in the peridotite could indicate that orthopyroxene crystallised at the expense of olivine (Jagoutz *et al.*, 2007).

The olivine pyroxenite hosts the most primitive orthopyroxene with xMg in the range of 0.84–0.86. Orthopyroxene in the peridotite ranges in xMg from 0.82 to 0.85 and the plagioclase-bearing olivine websterite from 0.78 to 0.83. The gabbro has the largest range of orthopyroxene compositions with xMg 0.74–0.83. There is an inflection point at xMg ~ 0.8, suggesting the beginning of plagioclase fractionation (Fig. 6d).

Table 1: EPMA mineral averages for the different lithologies. All oxides and totals are given in wt%

Olivine								
	Gabbro		Pl OlWeb		OlWeb		Peridotite	
	N = 2	2σ	N = 7	2σ	N = 14	2σ	N = 9	2σ
SiO_2	38.47	0.32	39.01	0.77	39.26	0.58	38.96	0.81
TiO_2	bdl	n/a	0.05	n/a	bdl	n/a	bdl	n/a
Al_2O_3	bdl	n/a	bdl	n/a	0.05	0.01	bdl	n/a
FeO^t	21.64	0.65	17.83	1.16	17.36	1.37	19.15	1.71
MnO	0.31	0.04	0.27	0.05	0.26	0.05	0.31	0.07
MgO	39.01	0.85	41.75	1.21	42.44	1.44	40.60	1.70
CaO	bdl	n/a	0.06	n/a	0.19	0.37	0.05	0.04
NiO	0.27	0.01	0.33	0.05	0.31	0.05	0.29	0.04
Total	99.76	0.51	99.27	1.12	99.85	0.79	99.40	0.95
Fo	*76.02*	*0.97*	*80.40*	*1.49*	*80.95*	*1.73*	*78.77*	*2.19*
$Fo = 100*Mg/(Fe^T + Mn + Mg + Ca)$								
Clinopyroxene								
	Gabbro		Pl OlWeb		OlWeb		Peridotite	
	N = 5	2σ	N = 66	2σ	N = 47	2σ	N = 6	2σ
SiO_2	52.66	2.42	52.89	2.22	52.83	1.59	54.91	1.07
TiO_2	0.49	0.67	0.38	0.44	0.32	0.39	0.10	0.04
Al_2O_3	2.29	1.61	2.11	1.32	2.02	1.09	2.70	1.07
FeO^t	7.22	3.02	5.98	1.73	5.19	1.85	4.49	0.34
Cr_2O_3	0.52	0.61	0.69	0.37	0.99	0.43	0.12	0.03
MnO	0.20	0.08	0.19	0.07	0.17	0.06	0.15	0.04
MgO	17.05	4.10	17.46	4.22	17.73	4.00	21.49	0.74
CaO	18.90	3.94	19.03	4.34	19.58	5.88	12.05	0.52
Na_2O	0.46	0.23	0.39	0.16	0.46	0.19	0.82	0.25
K_2O	bdl	n/a	0.06	n/a	bdl	n/a	0.07	0.03
NiO	0.07	n/a	0.08	0.02	0.08	0.01	0.09	0.03
Total	99.85	0.34	99.17	1.80	99.36	1.51	96.95	1.11
Wo	*39.19*	*8.52*	*39.72*	*10.09*	*40.59*	*12.52*	*26.51*	*1.21*
En	*49.09*	*10.50*	*50.53*	*10.55*	*51.05*	*10.39*	*65.77*	*1.65*
Fs	*11.72*	*5.22*	*9.74*	*2.93*	*8.37*	*2.79*	*7.72*	*0.66*
$Wo = 100*Ca/(Ca + Mg + Fe^T)$								
$En = 100*Mg/(Ca + Mg + Fe^T)$								
$Fs = 100*Fe^T/(Ca + Mg + Fe^T)$								
Orthopyroxene								
	Gabbro		Pl OlWeb		OlWeb		Peridotite	
	N = 4	2σ	N = 55	2σ	N = 39	2σ	N = 6	2σ
SiO_2	54.02	2.09	54.61	1.48	55.15	1.56	55.50	1.56
TiO_2	0.33	0.33	0.23	0.18	0.17	0.17	0.24	0.36
Al_2O_3	1.93	0.75	1.76	0.96	1.38	0.76	1.42	0.55
FeO^t	13.49	4.69	12.17	3.98	9.36	1.81	10.14	2.24
Cr_2O_3	0.23	0.19	0.30	0.18	0.54	0.18	0.50	0.29
MnO	0.32	0.07	0.28	0.08	0.24	0.06	0.25	0.07
MgO	27.27	3.30	27.77	2.51	30.19	1.44	29.74	1.17
CaO	2.04	0.58	2.06	1.67	2.24	0.73	1.77	1.42

Continued

Table 1: Continued

Orthopyroxene								
	Gabbro		Pl OlWeb		OlWeb		Peridotite	
	N = 4	2σ	N = 55	2σ	N = 39	2σ	N = 6	2σ
Na_2O	0.07	0.01	0.06	0.05	0.06	0.03	0.08	0.03
K_2O	bdl	n/a	0.03	n/a	0.05	n/a	bdl	n/a
NiO	0.07	0.00	0.10	0.04	0.10	0.03	0.10	0.03
Total	99.74	0.79	99.33	1.36	99.42	1.62	99.66	1.02
Wo	*4.04*	*1.00*	*4.10*	*3.33*	*4.36*	*1.37*	*3.47*	*2.78*
En	*75.31*	*6.45*	*76.99*	*5.61*	*81.98*	*2.33*	*81.02*	*1.86*
Fs	*20.65*	*7.45*	*18.92*	*6.47*	*13.65*	*2.80*	*15.52*	*3.59*
$Wo = 100*Ca/(Ca+Mg+Fe^T)$								
$En = 100*Mg/(Ca+Mg+Fe^T)$								
$Fs = 100*Fe^T/(Ca+Mg+Fe^T)$								

Plagioclase								
	Gabbro		Pl OlWeb		OlWeb		Peridotite	
	N = 3	2σ	N = 31	2σ	N = 0	2σ	N = 0	2σ
SiO_2	56.05	1.10	55.55	1.91				
TiO_2	0.07	0.03	0.07	0.03				
Al_2O_3	27.70	0.72	27.95	1.25				
FeO^t	0.21	0.19	0.22	0.23				
MgO	0.03	0.00	0.04	0.01				
CaO	9.90	0.82	10.32	1.56				
Na_2O	5.88	0.46	5.64	0.93				
K_2O	0.14	0.27	0.11	0.15				
SrO	0.12	0.06	0.11	0.07				
Total	100.11	1.22	100.00	1.09				
An	*47.85*	*4.08*	*49.97*	*7.72*				
$An = 100*Ca/(Ca+Na+K)$								

Amphibole								
	Gabbro		Pl OlWeb		OlWeb		Peridotite	
	N = 0	2σ	N = 10	2σ	N = 2	2σ	N = 0	2σ
SiO_2			45.63	4.95	42.66	0.45		
TiO_2			1.63	3.04	5.48	1.04		
Al_2O_3			11.20	2.72	11.58	1.03		
Cr_2O_3			0.20	0.22	0.84	0.13		
FeO^t			7.78	0.84	7.59	0.96		
MnO			0.14	0.11	0.19	0.17		
NiO + ZnO			0.12	0.04	bdl	n/a		
MgO			16.41	0.93	14.90	0.80		
CaO			11.67	0.43	11.30	0.32		
Na_2O			2.20	0.69	2.66	0.07		
K_2O			0.86	0.72	1.31	0.07		
F			0.05	0.04	0.02	0.02		
Cl			0.10	0.08	0.05	0.01		
Total			97.93	0.53	98.66	0.19		

Continued

Table 1: Continued

	Spinel							
	Gabbro		Pl OlWeb		OlWeb		Peridotite	
	N = 3	2σ	N = 15	2σ	N = 25	2σ	N = 27	2σ
SiO_2	0.13	n/a	0.43	n/a	bdl	n/a	bdl	n/a
TiO_2	0.37	0.19	1.62	1.32	3.79	13.66	0.96	0.78
Al_2O_3	9.29	1.22	6.22	4.56	12.08	4.99	7.33	8.62
Cr_2O_3	39.12	7.17	28.46	15.27	34.97	14.58	33.71	11.20
FeO^t	44.78	5.97	55.54	17.90	40.55	13.42	49.46	18.42
MnO	0.52	0.02	0.56	0.15	0.45	0.17	0.55	0.12
MgO	2.11	0.15	1.37	0.79	3.95	4.19	1.83	2.52
CaO	bdl	n/a	0.06	0.07	0.03	n/a	0.06	0.04
Na_2O	1.00	n/a	0.09	0.09	0.10	0.16	0.11	0.19
NiO	0.09	0.03	0.13	0.08	0.15	0.10	0.15	0.09
Total	96.70	0.62	94.01	1.75	95.98	1.40	94.11	2.18
apfu								
Ti	0.010	0.005	0.046	0.038	0.102	0.371	0.027	0.024
Al	0.391	0.053	0.272	0.192	0.501	0.200	0.315	0.359
Cr	1.104	0.199	0.838	0.425	0.972	0.379	0.985	0.276
Fe^{2+}	0.833	0.129	0.944	0.081	0.853	0.359	0.896	0.144
Fe^{3+}	0.505	0.131	0.797	0.532	0.393	0.255	0.649	0.543
Mg	0.113	0.009	0.076	0.042	0.206	0.211	0.099	0.130
xFe^2	*0.88*	*0.01*	*0.93*	*0.04*	*0.80*	*0.22*	*0.90*	*0.13*
xFe^3	*0.25*	*0.07*	*0.42*	*0.29*	*0.20*	*0.13*	*0.33*	*0.29*
xCr	*0.74*	*0.06*	*0.76*	*0.05*	*0.66*	*0.11*	*0.78*	*0.21*

$xFe^2 = Fe^2/(Mg + Fe^2)$
$xFe^3 = Fe^3/(Cr + Al + Fe^3)$
$xCr = Cr/(Cr + Al)$

End-member mole fractions or percentages in italics. 2σ represent the population's standard deviation; if N < 2, σ is not applicable (n/a).
Pl OlWeb, Plagioclase bearing olivine websterite; OlWeb, olivine websterite; bdl, below the detection limit; An, anorthite; Fo, forsterite; Wo, wollastonite; En, enstatite; Fs, ferrosilite; apfu, atoms per formula unit.

The intercumulus plagioclase in the ultramafic rocks ranges from An_{45} to An_{53}. The plagioclase of the melanocratic gabbro primarily lies within the andesine field with An_{33-49}. The amphiboles have xMg concentrations ranging from 0.77 to 0.80 and plot in the field of magnesio-hornblende and pargasite, together with a lesser amount of sadanagaite (Hawthorne *et al.*, 2012).

The ferric iron content of the spinels in this study is calculated according to stoichiometry (Deer *et al.*, 2013). The ferrous and ferric iron contents were estimated from the total FeO using the sum of charges in the ideal XY_2O_4 formula, where X = (Fe^{2+}, Ni, Mn, Co, Zn), Y = (Cr^{3+}, Fe^{3+}, Al) and Ti allocated to an ulvöspinel component.

The spinels classify as Al-chromite, ferrian chromite and Cr-magnetite, with the majority in the ferrian chromite field. Together, they show a trend of increasing ferric iron and evolve towards magnetite (Fig. 6e), correlated with a slight increase in TiO_2. The spinels are depleted in Al, Ni, Mg and Sc and show positive Ti and Zn anomalies when normalised to MORB chromites (Fig. 6f; Page & Barnes, 2009).

Oxy-thermobarometry

The pressure and temperature were estimated based on the single-phase (amphibole) empirical thermobarometric formulation (±22°C and c. ±40 MPa) of Ridolfi *et al.* (2009), the two-pyroxene thermobarometric formulations (c. ±42°C and ± 280 MPa) of Putirka (2008) and the two-pyroxene thermometer (±50°C) of Brey & Köhler (1990). The individual estimates together with standard deviations can be found in Supplement 5.

There is a substantial variation in pressure and temperature estimates based on mineral chemistry (Fig. 7a). The densest locus in P/T space is around 400 MPa and 1000°C, with a tail of estimates along the dry peridotites solidus of Hirschmann (2000). The highest estimated pressures and temperatures are for the two-pyroxenes in the peridotites (~900 MPa, ~1250°C). However, as Fig. 6c shows, a slight Fe–Mg disequilibrium might affect this estimate.

Even disregarding the peridotites, there is still a considerable variation in pressure and temperature, which could indicate that crystallisation commenced in a staging magma chamber at depth. Geothermometers calibrated on Mg–Fe^{2+} exchange in olivine–spinel mineral pairs (Ashchepkov *et al.*, 2008) yield higher temperature estimates (Fig. 7b). Spinel commonly occurs as inclusions in olivine and likely was the first phase to crystallise and, therefore, is expected to record higher temperatures.

The spinel–olivine–orthopyroxene oxygen sensor (Ballhaus *et al.*, 1990) estimates fugacities between ~3.3 and 3.5 log f_{O2} ΔQFM (Fig. 7b; Frost, 1991). Such high oxygen fugacities are uncommon and primarily documented in xenoliths entrained in ocean island basalts (Cottrell *et al.*, 2021). We note that our estimates must be viewed as semi-quantitative as the spinel $Fe^{3+}/\sum$Fe-ratio is calculated by ideal stoichiometry without any calibration standards (Birner *et al.*, 2018).

Table 2: Spinel LA-ICP-MS averages for the different lithologies in parts per million (ppm)

	Pl OlWeb		OlWeb		Peridotite	
	N = 2	2σ	N = 4	2σ	N = 8	2σ
Li	*bdl*	n/a	7	n/a	8	2
Mg	15 028	3451	50 789	13 211	14 738	46 259
Al	61 245	9901	62 200	3091	64 525	17 463
Ca	302	n/a	381	227	*bdl*	n/a
Sc	2	1	3	1	2	7
Ti	3144	1814	5609	1007	4827	2727
V	1434.6	52.5	1368.6	360.0	1878.5	314.7
Cr	327 398	88 288	321 372	37 114	262 530	47 710
Mn	4077.3	1585.7	2567.0	604.8	3902.5	1432.4
Fe	353 676	23 319	237 080	20 195	390 599	110 954
Co	615.4	34.1	508.2	122.5	657.4	272.6
Ni	654	200	1091	402	1317	844
Cu	2	n/a	*bdl*	n/a	2	1
Zn	8072	2985	1056	186	4619	7045
Ga	51.5	10.6	48.4	6.2	92.2	45.1
As	0.3	n/a	1.0	1.5	0.3	n/a
Nb	0.18	0.06	0.20	0.05	0.15	0.06
Cd	*bdl*	n/a	*bdl*	n/a	0.3	0.1
Sn	*bdl*	n/a	0.3	0.2	0.2	0.7
Sb	*bdl*	n/a	*bdl*	n/a	0.07	0.04
Re	*bdl*	n/a	0.02	n/a	*bdl*	n/a
Ir	0.09	0.07	0.04	0.01	0.02	0.02
Pt	0.04	n/a	0.03	0.07	0.02	0.02
Tl	0.02	n/a	*bdl*	n/a	0.01	n/a
Pb	0.38	0.71	0.04	0.01	1.81	3.72
Bi	0.03	n/a	*bdl*	n/a	0.02	n/a

2σ represent the population's standard deviation; if N < 2, σ is not applicable (n/a).
Pl OlWeb, Plagioclase bearing olivine websterite; OlWeb, olivine websterite; bdl, below the detection limit.

Whole-rock major, minor and trace elements

Table 3 gives a summary of the whole-rock results acquired in this study. The ranges reported here are the groups' statistical variation with outliers excluded (cf. section on mineral chemistry). The complete dataset is presented in Supplement 6.

Selected major element oxides are presented in Fenner diagrams in Fig. 8 and downhole in Fig. 4. There is only minor variation in the major element oxide concentrations of the ultramafic rocks. The most primitive peridotites have major and minor element concentrations like the orthopyroxene average (Fig. 8b–f) and the group lies along a clinopyroxene–orthopyroxene mixing line. There is an inflection point between 20 and 25% MgO in the major and minor element data. The olivine websterites first show this change towards higher aluminium, alkalis and lower calcium with decreasing MgO (Fig. 8c–e), consistent with plagioclase accumulation. Biotite, amphibole and Fe–Ti oxide likely control the inflection in the TiO_2 vs MgO diagram (Fig. 8f), consistent with common rutile exsolutions in biotite (Fig. 5j,k). The dolerites are not distinct from the evolved gabbro major and minor element compositions (Fig. 8). However, these two rock types are distinctly different when considering the Rare Earth Elements (REE) and other trace elements (Figs 9 and 10). The dolerite and gabbro have similar LREE $(La/Sm)_N$ trends, but the dolerites consistently have lower HREE $(Gd/Yb)_N$. The dolerites have Nb/Th ratios between 5.2 and 6.0, close to the primitive mantle ratio (~8.4; Sun & McDonough, 1989), while the other lithologies have Nb/Th ratios ranging from 0.4 to 2.4 (Fig. 9c). The latter ranges are more consistent with average crustal values (~2.3; Weaver & Tarney, 1984). The difference in Nb/Th ratio between the dolerites and the other lithologies could be related to the extent of crustal assimilation (Pilet *et al*., 2004), although isotopic data are needed to verify this assertion. Another feature to note is the near linear drop in Ni with decreasing MgO (Fig. 9d).

Figure 10 shows primitive mantle- and chondrite-normalised averages for the lithologies of the intrusion and arenitic host rock, as well as the average of two granodiorite samples from the Jergul Complex. All the lithologies of the Gallujavri intrusion show many similar features in the multi-element diagram, such as large-ion lithophile (LILE) and LREE enrichment, positive W, U and Pb and negative Nb–Ta, P, Eu and Ti anomalies normalised to primitive mantle (Fig. 10a). The dolerites break up this pattern with a more pronounced negative Ta and less pronounced positive Pb and negative P anomalies. All the ultramafic cumulates of the Gallujavri intrusion have similar REE patterns when normalised to chondrite (Fig. 10b; Sun & McDonough, 1989) with average $(La/Yb)_N$ ranging from 2.5 to 3.2. With respect to the REEs, the gabbros are most fractionated with average $(La/Yb)_N = 4.9$ and the least fractionated are the dolerites with $(La/Yb)_N = 2.1$. The igneous rocks mimic many features present in the arenite and Jergul Complex, most evident in the Th, U, Nb, Ta, K and Pb anomalies.

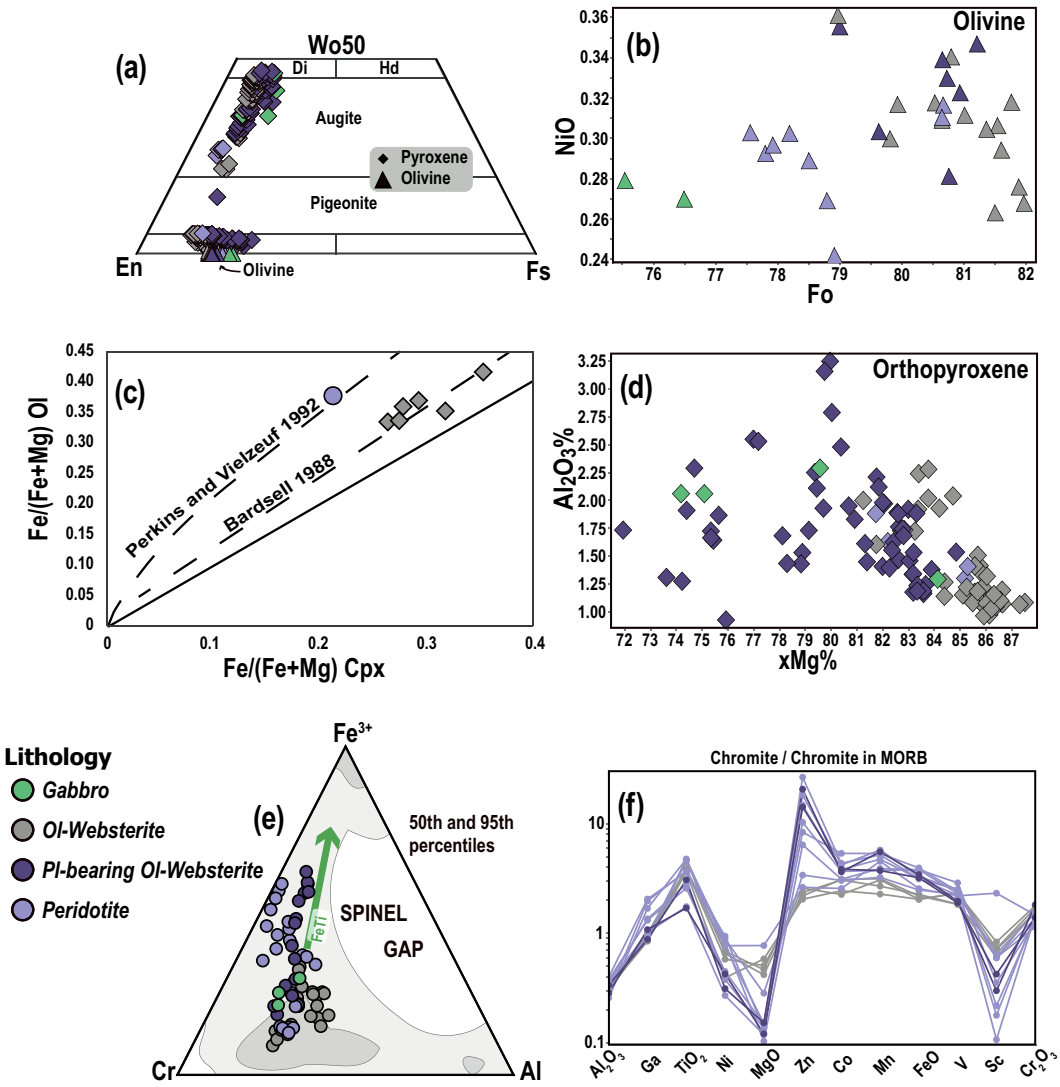

Fig. 6. Mineral chemistry and classification diagrams. (a) Pyroxene trapezoid with (end)members diopside (Di), enstatite (En), ferrosilite (Fs) and hedenbergite (Hd). Augite dominates the clinopyroxene compositions, with a small high-Ca fringe classified as diopside. Orthopyroxene clusters around En_{80} with $Wo_{0–5}$. Olivine (triangles) is included in the diagram and plot along the En–Fs join. (b) Olivine NiO vs Fo%. (c) Graph of xFe (Fe/(Fe + Mg)) in olivine (Ol) and clinopyroxene (Cpx) relative to the equilibrium curves of Barsdell (1988) and Perkins & Vielzeuf (1992). Olivine websterites in grey follow the curve of Barsdell (1988), the olivine–clinopyroxene pair from the peridotite (light blue) plots separately and slightly above the curve of Perkins & Vielzeuf (1992). (d) Al_2O_3 vs xMg% variation diagram for orthopyroxene showing a weak negative and positive correlation for xMg% > 80 and <80, respectively. (e) Ternary diagram relating our analysed spinels to the Fe–Ti trend (green arrow) and compositional fields as defined by Barnes & Roeder (2001) for spinels from mafic–ultramafic igneous rocks. (f) Analysed spinel major, minor and trace elements normalised to MORB chromites (Page & Barnes, 2009).

DISCUSSION

Modelling assumptions and parameters

Komatiitic and basaltic volcanism in the KCLGB coeval with the Gallujavri intrusions suggests that the intrusion may represent a magma conduit in an intracontinental rift (Often, 1985; Krill, 1985b; Barnes & Often, 1990). This hypothesis is consistent with previous models proposed for the Palaeoproterozoic komatiite–picrite association of the Fennoscandian Shield (Krill, 1985a; Barnes & Often, 1990; Hanski *et al*., 2001a), and the spinel compositions yield similar trends to those documented for subvolcanic intrusions in the Siberian and Karoo flood basalt provinces (Barnes & Roeder, 2001). This spinel Fe–Ti trend likely results from the co-fractionation of spinel with olivine or pyroxene from the parental melt (Fig. 6e; Barnes & Roeder, 2001, Irvine, 1967). In combination with the parental melt evolution, the variation of xFe^{2+} in spinel likely results from the temperature-dependent partitioning of Mg and Fe^{2+} ($K_D(Mg–Fe^{2+})$) between spinel and silicates. This equilibrium favours increased xFe^{2+} in spinel with decreasing temperature, an effect that is most pronounced in rocks that cooled slowly (Irvine, 1965; Irvine, 1967; Barnes & Roeder, 2001). The major, minor and trace element trends are characteristic and comparable to spinel compositions documented for continental mafic intrusions and subvolcanic mafic intrusions from continental flood basalt terrains (Fig. 6f; Barnes & Roeder, 2001). The most commonly proposed model for forming these large igneous provinces is the partial melting of a mantle plume or the impingement of a mantle plume at the base of the crust (Lightfoot *et al*., 1993; Duncan *et al*., 1997;

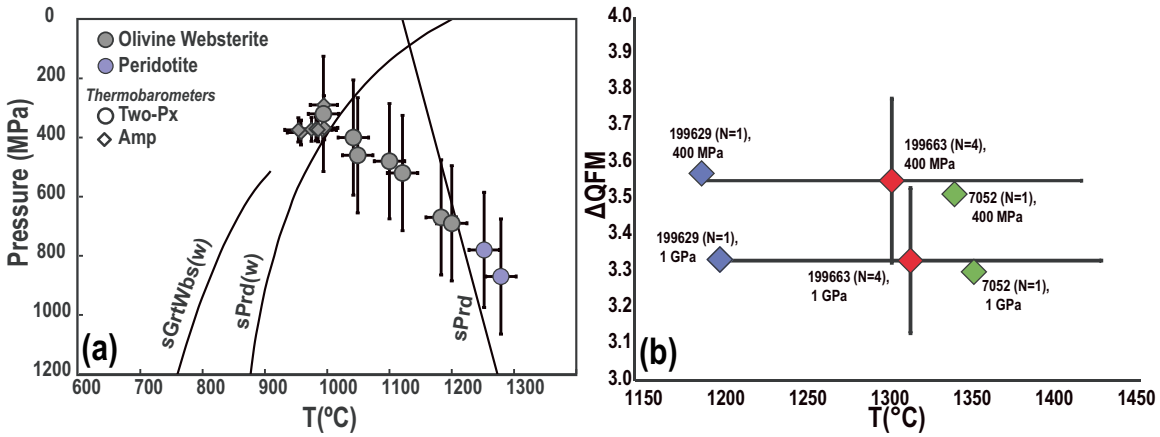

Fig. 7. Oxy-thermobarometric estimates. (a) Amphibole, orthopyroxene and clinopyroxene thermobarometry. Mineral pairs from peridotites in light blue. Mineral pairs from olivine websterites in grey. Diamonds: amphibole thermobarometer (Ridolfi *et al.*, 2009). Circles: weighted averages of the two-pyroxene thermometer of Brey & Köhler (1990) and the two-pyroxene thermobarometers of Putirka (2008). Reference lines: anhydrous solidus for peridotite (sPrd; Hirschmann, 2000), hydrous peridotite solidus (sPrd(w); Boettcher *et al.*, 1975) and hydrous garnet websterite solidus (sGrtWbs(w); Mysen & Boettcher, 1976). (b) Olivine–spinel thermometer (Ashchepkov *et al.*, 2008) and olivine–spinel–orthopyroxene oxybarometer (Ballhaus *et al.*, 1990) relative to the QFM reference buffer of Frost & McCammon (2008). The fugacity is estimated for mineral pairs from three samples: 199629 (blue diamonds; N = 1), 199 663 (red diamonds; N = 4), and 7052 (green diamonds; N = 1) assuming pressures of 400 and 1000 MPa. For sample 199 663, the error bars signify the standard deviation of the population of estimates.

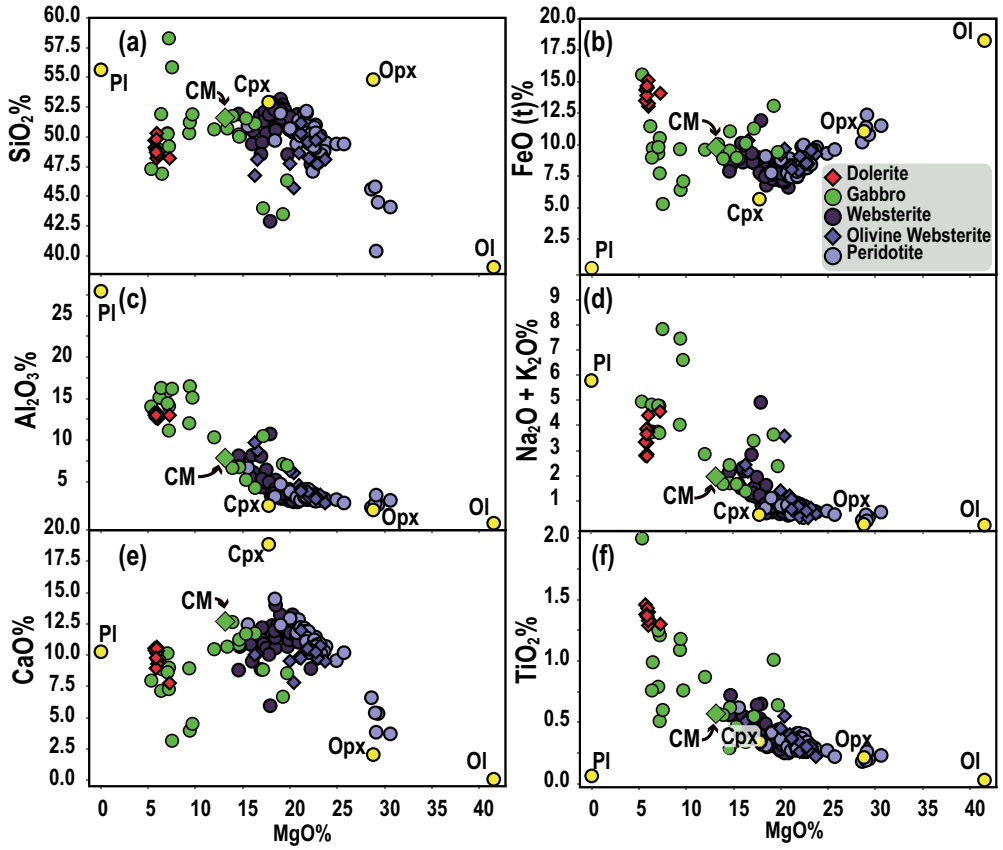

Fig. 8. Major and minor whole-rock Fenner diagrams (wt%) for rocks of the Gallujavri intrusion. Filled yellow and labelled circles mark average mineral EPMA analyses. Pl, plagioclase; Cpx, clinopyroxene; Opx, orthopyroxene; Ol, olivine.

Ernst & Jowitt, 2013, consistent with the proposed models for the Palaeoproterozoic komatiites in the KCLGB (Barnes & Often, 1990; Puchtel *et al.*, 1998; Hanski *et al.*, 2001a; Puchtel *et al.*, 2020).

The high potential temperature of komatiitic melts makes them highly susceptible to contamination by crustal material (Huppert & Sparks, 1985). As noted previously, the KCLGB komatiites are characteristic in that they are enriched in Ti and other high field strength elements relative to typical komatiites (Barnes & Often, 1990; Hanski *et al.*, 2001a). Barnes & Often (1990) dismissed crustal assimilation to explain the Ti- and LREE enrichment of the

Table 3: Whole-rock averages for different lithologies in weight percent (wt%) oxides (+LOI) and parts per million (ppm) elemental traces

	Arenite		Dolerite		Gabbro		Websterite		OlWeb		Peridotite	
	$N = 7$	2σ	$N = 11$	2σ	$N = 10$	2σ	$N = 8$	2σ	$N = 6$	2σ	$N = 18$	2σ
SiO_2	65.5	10.7	48.9	1.3	48.3	5.4	49.5	5.5	48.0	2.5	48.0	5.7
Al_2O_3	15.82	3.74	12.97	0.46	11.09	8.10	4.55	5.12	4.48	4.45	3.07	1.95
$Fe_2O_3{}^T$	6.80	3.43	15.77	1.48	12.28	4.13	9.97	3.30	10.45	1.26	10.78	2.59
CaO	2.60	3.12	9.82	1.68	9.64	3.39	10.79	4.23	9.76	1.96	9.56	6.29
MgO	2.10	1.92	6.01	0.82	11.27	10.12	19.09	3.58	21.46	4.87	23.97	8.07
Na_2O	3.27	2.39	2.75	0.69	2.23	2.12	0.67	0.64	0.62	1.07	0.47	0.48
K_2O	1.88	1.24	0.81	0.69	1.14	1.50	0.75	2.51	0.65	2.35	0.12	0.17
Cr_2O_3	0.029	0.010	0.011	0.004	0.173	0.429	0.502	0.320	0.453	0.249	0.562	0.218
TiO_2	0.72	0.58	1.37	0.10	0.91	0.98	0.36	0.23	0.33	0.22	0.28	0.19
MnO	0.06	0.07	0.25	0.06	0.16	0.05	0.16	0.02	0.17	0.07	0.18	0.03
P_2O_5	0.06	0.05	0.11	0.01	0.08	0.09	0.02	0.01	0.02	0.02	0.02	0.03
LOI	1.27	0.46	0.76	1.06	1.45	1.09	2.54	1.55	3.01	2.90	2.54	4.39
Total	100.18	1.01	99.62	1.71	98.75	3.22	98.89	1.69	99.38	1.16	99.54	1.85
Cs	2.38	1.50	0.26	0.17	1.83	5.06	1.17	3.80	1.62	6.20	0.23	0.22
Rb	80	38	24	27	43	81	28	98	30	121	4	6
Ba	514	457	228	170	275	218	137	400	98	313	36	45
Th	7.73	3.60	0.90	0.13	1.85	1.81	0.93	2.63	0.36	0.36	0.38	0.36
U	1.87	1.06	0.30	0.04	0.56	0.35	0.33	0.26	0.19	0.19	0.12	0.10
Nb	6.8	3.6	5.0	0.6	2.3	2.2	0.8	1.1	0.7	0.8	0.7	2.0
La	26.6	18.7	7.2	0.5	8.6	8.8	2.6	5.1	2.5	4.8	2.2	2.3
Ce	51.2	34.1	16.7	1.3	17.9	16.2	5.6	9.9	4.7	6.9	4.6	4.7
Pb	5	6	4	4	9	19	4	7	4	8	5	11
Pr	6.06	3.81	2.47	0.16	2.40	2.03	0.83	1.13	0.65	0.68	0.67	0.64
Sr	252	126	152	31	171	226	21	27	42	81	33	40
Nd	22.7	13.9	11.9	1.1	10.9	8.9	4.0	4.0	3.1	2.3	3.2	2.8
Sm	3.80	2.17	3.21	0.35	2.63	2.28	1.15	0.83	0.95	0.53	0.85	0.71
Zr	197	131	76	6	85	73	27	36	41	98	18	16
Hf	5.4	3.4	2.3	0.3	2.4	2.0	0.7	0.9	1.1	2.2	0.6	0.5
Eu	1.02	0.49	1.12	0.22	0.91	0.74	0.33	0.22	0.30	0.21	0.27	0.23
Gd	3.29	1.85	3.80	0.54	3.07	2.79	1.35	0.78	1.06	0.44	1.04	0.70
Tb	0.47	0.22	0.67	0.08	0.48	0.44	0.22	0.10	0.19	0.06	0.17	0.11
Dy	2.62	1.55	4.11	0.41	2.76	2.30	1.36	0.64	1.07	0.34	1.01	0.69
Li	13	9	15	13	14	10	20	28	15	10	10	n/a
Y	14.5	8.1	23.4	2.2	14.7	12.5	7.1	4.1	5.9	2.4	5.2	3.3
Ho	0.53	0.26	0.92	0.07	0.54	0.46	0.29	0.17	0.22	0.08	0.20	0.13
Er	1.43	0.72	2.56	0.30	1.48	1.28	0.77	0.51	0.60	0.19	0.54	0.34
Tm	0.21	0.09	0.37	0.05	0.21	0.18	0.12	0.07	0.08	0.03	0.08	0.06
Yb	1.28	0.44	2.33	0.21	1.17	0.75	0.60	0.56	0.52	0.23	0.45	0.29
Lu	0.20	0.08	0.37	0.06	0.19	0.13	0.11	0.08	0.08	0.04	0.07	0.05
Ga	21.01	5.98	18.30	2.15	17.16	12.31	7.73	7.34	7.27	5.72	5.35	2.72
V	143	137	377	19	250	221	106	104	94	57	62	64
Co	28	21	53	4	76	64	78	61	80	16	99	48
Cu	50	71	145	85	621	1928	606	1298	211	276	463	1743
Ni	81	42	56	12	653	1738	889	577	714	233	1155	987
Sc	14	7	43	2	26	18	33	6	27	11	28	14
Zn	54	46	94	32	81	55	60	13	55	16	53	22

2σ represent the population's standard deviation; if $N < 2$, σ is not applicable (n/a).
OlWeb, olivine websterite.

Karasjok komatiites as crustal material is too SiO_2-rich and has too high Al_2O_3/TiO_2 ratios. Later, Hanski (2001a) confirmed that the same conclusions apply to the komatiites and picrites of Jessiörova and the Peuramaan area of Finnish Lapland.

Based on the available regional geological, geochronological and geochemical data, we hypothesise the following:

(1) The spatial and temporal links between the Gallujavri ultramafic intrusion and the subaerial komatiites of the KCLGB imply that they form a cognate magma system. We hypothesise that the Gallujavri intrusion represents part of the volcanic plumbing system that fed the overlying volcanic rocks.

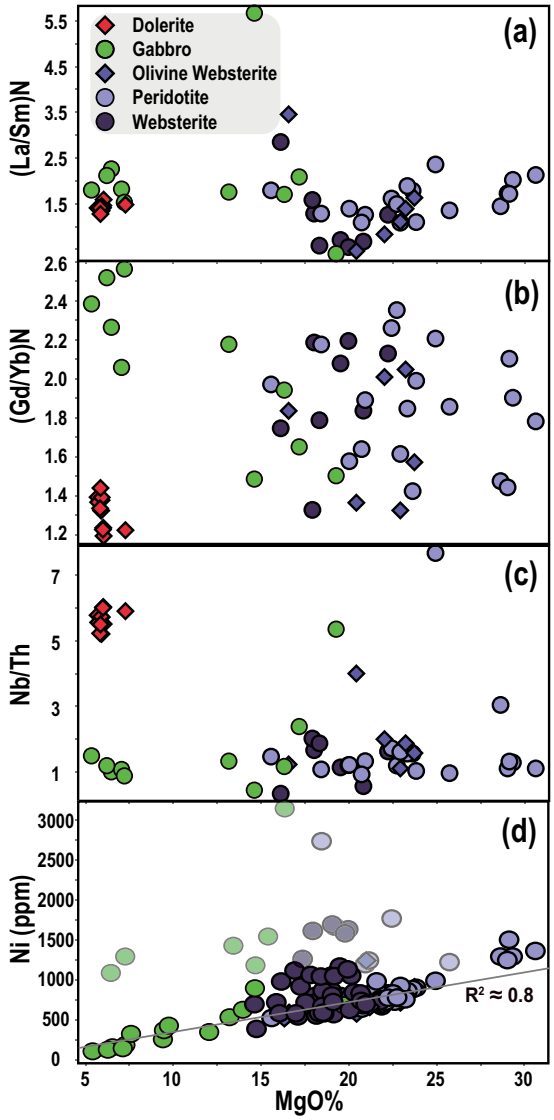

Fig. 9. REE chondrite-normalised (Boynton, 1984) ratios, Nb/Th ratio and Ni (ppm) vs MgO (wt%) for rocks of the Gallujavri intrusion. The Ni vs MgO diagram includes a least-squares linear regression line of the highlighted samples with a slope of 45.7 and intercept of 143.9 ($R^2 = 0.77$).

(2) There is clear evidence of contamination in the primitive mantle-normalised multi-element patterns, such as enrichment in LILE and LREE with positive U and Pb and negative Nb–Ta, Ti and Eu anomalies. Moreover, the stratigraphically uniform and consistently low Nb/Th-values indicate that the assimilation occurred in a staging magma chamber, where melts were partly homogenised before further ascent.

(3) A polybaric evolution is implied from our pressure estimates (Fig. 7a) that show a cluster at 400 MPa and a tail towards 700 MPa.

In the following, we present models to test these hypotheses. We subdivide our model into two stages (Fig. 11). In the first stage, we will test whether the Palaeoproterozoic komatiites of the KGB, as documented by Barnes & Often (1990), represent an analogue to the parental melt of the Gallujavri intrusion. Here, our goal is to model mineral chemistry and to examine whether AFC at 700 MPa can produce an evolved melt consistent with our CM (cf. sample 199 610; Fig. 4b).

The second stage is to model the mineral chemistry and liquid evolution of more evolved mafic whole-rock samples using the CM as the starting composition. The second-stage model assumes that the later assimilation and fractionation occurred at 400 MPa, as indicated by our pressure estimates.

Parental melt composition

The high MgO contents of the Karasjok komatiites imply high degrees of mantle melting, thus they probably approach the mantle source composition. The primitive nature and the interpretation that the Karasjok komatiites are negligibly affected by assimilation and crystal fractionation *en route* to the subsurface (Barnes & Often, 1990) make them an ideal starting composition for our models.

The primitive melt composition used in the first-stage model is taken from the geochemical data reported for three komatiitic pillow lavas in the KGB (Barnes & Often, 1990; X [M4383, DAT1/5, DAT1/8]). M4383 represents pillow lava from a 10-m-thick flow, DAT1/8 pillow interior from a 15-m-thick flow and DAT1/5 from the same pillow but at the rim. The samples are thought to represent liquid compositions as the compositions of pillow interiors and rims are similar. There is, however, evident secondary alteration with elevated $H_2O + CO_2$ concentrations ranging between c. 10% and 16%. Elements with low ionic potential, such as Rb^+, K^+, Na^+, Sr^{2+}, Eu^{2+} and Ca^{2+}, are the most susceptible to alteration in komatiites (Beswick, 1982; Ludden *et al.*, 1982; Barnes, 1985; Barnes & Often, 1990), and the three samples display irregular behaviour concerning most of these elements in mantle-normalised plots (Barnes & Often, 1990).

The parental melt (M) used as the starting composition in the first stage is the average of the three samples ($\bar{x}$; Table 4), the exceptions being H_2O, Eu (maximum value) and Sr (minimum value). Two of the samples have negative Eu anomalies that are most likely due to secondary alteration (Sun & Nesbitt, 1978; Hanski *et al.*, 2001a). There is also variation in the LILE concentrations (e.g. Sr), probably due to enrichment related to hydrothermal alteration (Frey & Green, 1974; Sun & Nesbitt, 1978).

Since the Fe oxidation state is undetermined, we calculated the Fe^{2+}/Fe^t ratio relative to the QFM buffer at the model pressure (700 MPa) and liquidus temperature ($T^{\bar{x}}_0 = 1698°C$, see below) using the MELTS_Excel interface (Gualda & Ghiorso, 2015) – no oxygen redox buffer was used in the runs themselves.

The volatile content of the parental melt is also unknown and there is much debate regarding the volatile budget of komatiites. Many maintain that komatiitic lavas were essentially dry, while others assert that komatiites contained several wt% water, in effect drastically reducing eruption temperatures (Arndt *et al.*, 1998; Sobolev *et al.*, 2016). As the Palaeoproterozoic komatiites of the KCLGB most likely have a mantle plume origin (Barnes & Often, 1990; Puchtel *et al.*, 1998; Hanski *et al.*, 2001a; Puchtel *et al.*, 2020), we used an H_2O/Ce-ratio of c. 600 ($\bar{x}\ H_2O = 0.2\%$), which is about average between MORBs and the ranges documented for continental flood basalts (Karoo, Tarim, Snake River Plain and the Permian Emeishian LIP; Heinonen *et al.*, 2019, Liu *et al.*, 2017).

In the second stage, the CM was used as the starting melt (Table 5). Like the first stage, the Fe oxidation state is undetermined. We computed the redox state relative to the QFM buffer as we did before, but at the estimated liquidus temperature of the CM ($T^{CM}_0 = 1273°C$, see below) at 400 MPa. Although we determined

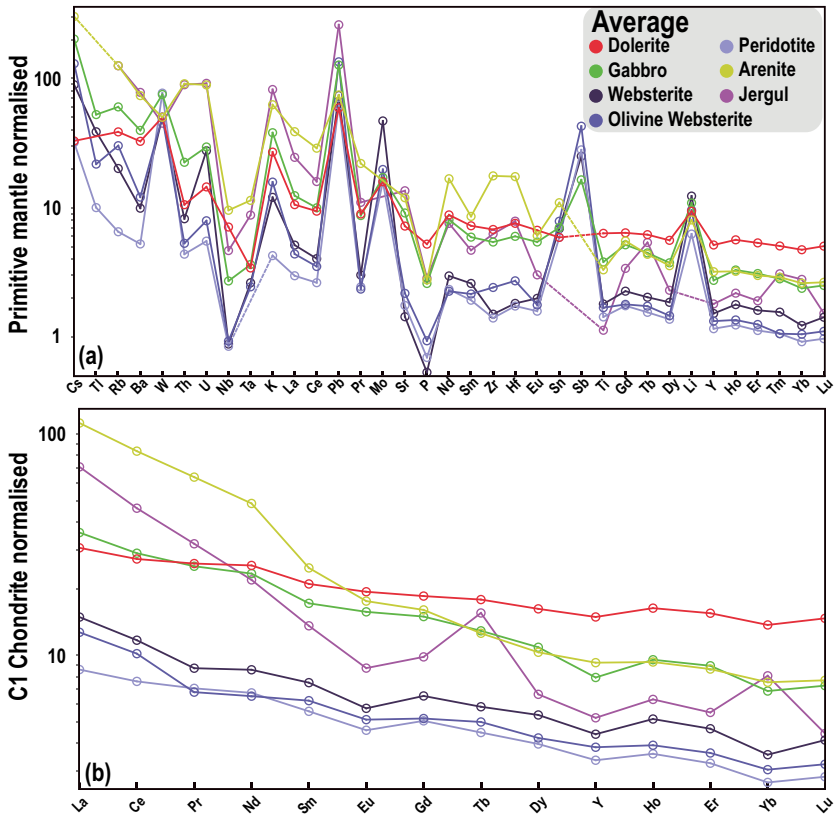

Fig. 10. (a) Multi-element primitive mantle-normalised (Sun & McDonough, 1989) diagram showing average compositions of the different rock types. (b) REE C1 Chondrite-normalised diagram for average compositions of the different rock types (Sun & McDonough, 1989).

the loss on ignition (LOI) during our whole-rock analysis (CM LOI =0.81), we normalised the oxide composition with 1 wt% water. This assumption is justified because the modelled melt compositions in stage 1 are in that range of water concentrations at similar MgO contents as the CM.

Plagioclase, orthopyroxene and clinopyroxene must be stable under this modelling stage, as indicated from petrography and the c. 400 MPa Mg–Fe equilibrium. However, orthopyroxene is not a liquidus phase of our CM at this pressure. In order to stabilise orthopyroxene in this stage, there must be an addition of a melt of different composition, therefore at 1050°C, 75 mass units (m.u.) of $\bar{x}$ (i.e. stage 1 parental melt) is recharged (Fig. 11), consistent with the presence of inferred komatiitic stage 1 parental melt erupting at the surface.

Mineral–melt partition coefficients in both stages were collected from the EarthRef database (https://earthref.org/KDD) for mafic to ultramafic melt compositions. When partition coefficient data were missing, the value was set as the MCS default or 1. The partition coefficients are listed in the MCS output files, and the individual references can be found in Supplement 7.

Wall-rock compositions

In the first stage, the source of crustal contamination is assumed to be that of the Jergul Complex, represented by sample 127 363 (Table 4). The Jergul Complex is an Archaean cratonic block of Karelian affinity, made of variably gneissic TTG plutonic rocks formed between 2975 ± 10 and 2776 ± 6 Ma (Bingen *et al.*, 2015). Sample 127 363 is a weakly peraluminous normative granodiorite. When used as the WR composition, the sample was normalised with a Fe oxidation state related to the QFM buffer close to the solidus temperature (780°C) at the model pressure of 700 MPa and a water concentration of 0.4 wt%.

In the second stage, the crustal contaminant is assumed to be the arenite host to the Gallujavri intrusion. The WR was initialised as the average of the arenitic samples documented in this study. The average was then normalised with a Fe oxidation state calculated as before (685°C, 400 MPa) and 1 wt% water.

The partition coefficients for the wall rock in both stages were collected from the EarthRef database for listed felsic compositions. The MCS output files show the partition coefficients and the individual references can be found in Supplement 7.

Pressure, temperature and mass constraints

As discussed above, we assume a polybaric evolution of the system, the first stage with a pressure of 700 MPa, representing a depth of c. 25 km assuming a crustal density of 2800 kg/m^3, and the second stage at 400 MPa (depth of c.15 km). In the first stage, the wall-rock temperature was initially at 700°C ($T_{solidus}$ ~ 780°C), giving a close-to-average crustal geothermal gradient of ~28°C/km. In the second stage, the wall rock was initially at 650°C ($T_{solidus}$ ~ 685°C), giving a geothermal gradient of ~46°C/km. We assume that previous magma pulses had already heated the wall rocks before the second stage.

In our models, the mass of the parental melt was always set to 100 m.u. (default) and the wall-rock masses in stages one and two were set to 300 m.u. Our hypothesised polybaric conduit system

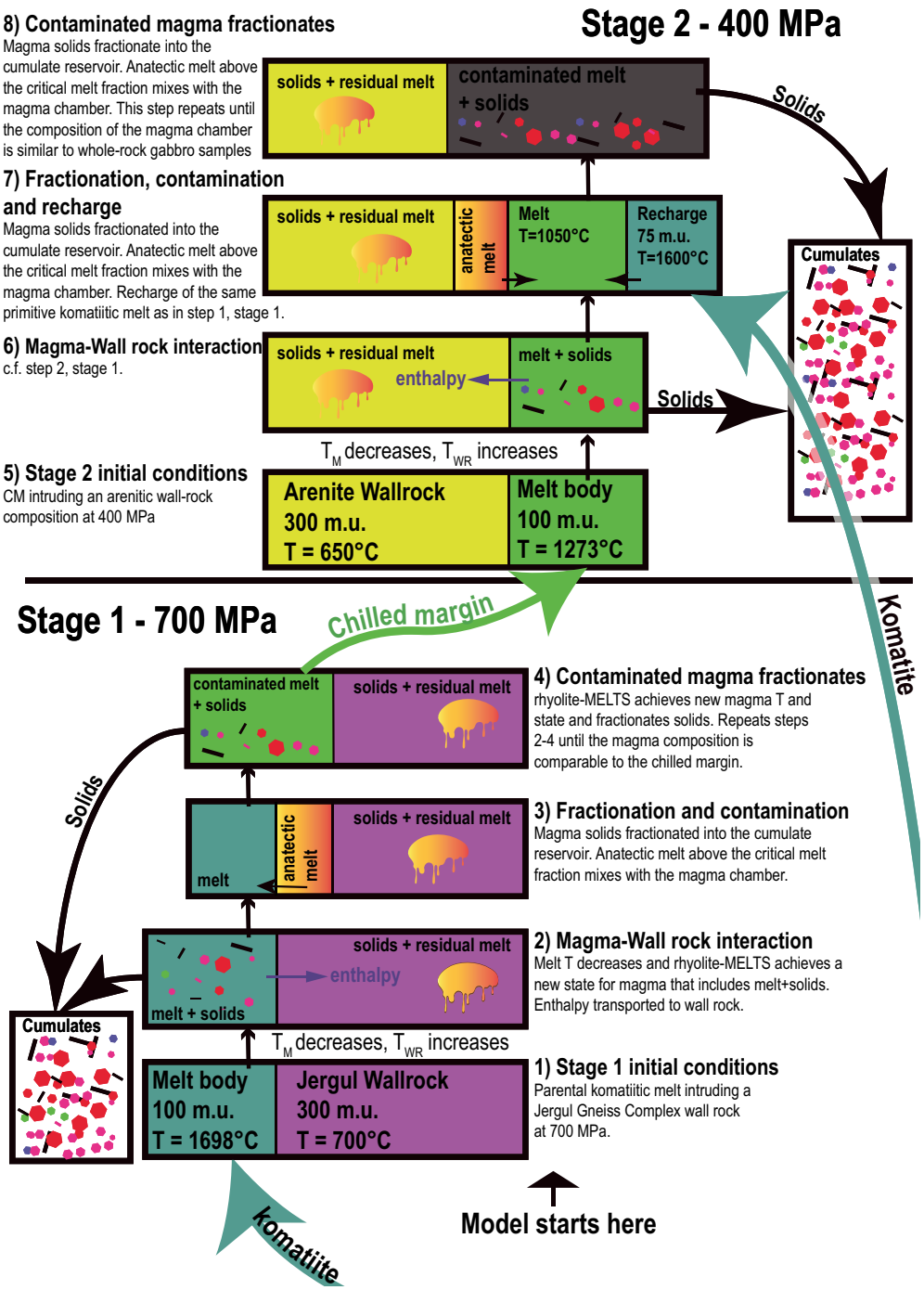

Fig. 11. Schematic illustration of the petrogenetic model, modified from Bohrson *et al*. (2014). m.u., mass unit.

suggests that the magma could have a high surface area towards heated crustal material (e.g. magma pipe). In total, along the transport direction, the surface would release a relatively high proportion of low-degree anatectic melt. The chosen masses mean that the heat available from the initial melt can thermally interact with three times as much wall-rock mass as the original intruding magma (i.e. $\Lambda = 3$). A mass ratio of three is justified because the surface-to-volume ratio increases with divergence from a sphere, increasing reactivity. Also, the enthalpy generated by the crystallisation of mafic mineral phases (spinel, olivine, clinopyroxene) is higher by a factor of two than the fusion enthalpy of the felsic phases in the wall rock (Bohrson *et al*., 2020).

As in all modelling-based studies, the results obtained are variably contingent on a range of assumptions and choices of conditions and parameters. Therefore, such a study would not be complete without assessing the significance of these assumptions and choices on the

Table 4: Stage 1 parental melt (M) and wall-rock (WR) compositions and parameters

	M ($\bar{x}$)	WR (127363)
SiO_2	43.6	75.7
TiO_2	0.8	0.3
Al_2O_3	6.3	10.8
Fe_2O_3	2.3	0.8
Cr_2O_3	0.5	0.005
FeO	9.9	2.7
MnO	0.2	0.04
MgO	25.3	2.0
NiO	0.2	0.002
CoO	0.01	0.001
CaO	10.5	2.0
Na_2O	0.1	3.3
K_2O	0.02	1.8
P_2O_5	0.04	0.1
H_2O	0.2	0.4
Sc	27.6	8.8
V	314	50.8
Rb	2.5	58.1
Sr	75*	160
La	0.6	15.4
Ce	3.4	27.7
Nd	2.8	11.9
Sm	1.4	3
Eu	0.38**	0.7
Tb	0.3	0.6
Ho	0.3	0.6
Lu	0.1	0.2
Hf	0.8	3
Th	0.1	8.3

	FC: Melt	Wall rock	AFC: Melt
Pressure (MPa)	700	700	700
Mass (m.u.)	100	300	
Decrement, ΔT(°C)	20		20
Initial wall-rock T (°C)		700	
FmZero		0.05	

The parental melt (M) represents the average ($\bar{x}$) of three pillow komatiite samples (X = DAT 1/5, DAT 1/8, M4383) and a Jergul Gneiss Complex wall rock. The exception from the average includes *MIN(X) and **MAX(X). All oxides are reported in wt%, and all trace elements are reported in ppm.

model results. To this end, supplement 8 presents a sensitivity analysis in which we show and discuss the effects of varying the model inputs.

Modelling results

Stage 1 (700 MPa)

Supplement 9 presents the modelled cumulate stratigraphy. Modelled major element compositions are presented in Fig. 12 and trace element compositions in Fig. 13.

The parental magma initially has a liquidus temperature of $T^M_0 \sim 1698°C$; upon cooling, olivine and spinel crystallise at a ratio of c. 23:1. When the melt has cooled to a temperature of 1460°C, the melt fraction of the wall rock exceeds the percolation threshold of 0.05, releasing 2.93 m.u. of anatectic melt to the magma chamber.

Relative to FC-only models, the addition of anatectic melt increases the SiO_2 and H_2O of the magma chamber melt and decreases MgO and FeO. Another essential feature is that the addition of Si from the wall rock to the resident magma stabilises orthopyroxene, which starts to crystallise at 1374°C. Clinopyroxene stabilises at 1298°C. When the resident magma has a temperature of 1278°C and MgO = 11.4 wt% (cf. CM MgO = 12.0 wt%), the melt has assimilated about 15 m.u. of anatectic melt.

The modelled trace element concentrations presented in Fig. 13 represent the model interval (12–18 wt% MgO; 1298–1410 T^M(°C)) highlighted by orange ticks in Fig. 12. Figure 13a shows that there is a general agreement between the composition of the CM and the model melts of stage 1, although modelled concentrations of Rb, Th K, Hf and Ti are somewhat too high. These features are also evident in Fig. 13b but with a good overall match with the observed La/Lu trend.

The transition metals show more significant deviations (Fig. 13c), and although the primitive mantle-normalised modelled patterns are

Table 5: Stage 2 parental melt (M), wall rock (WR) and recharge (R) compositions and parameters

	M (199610)		WR (Arenite)	R ($\bar{x}$)
SiO_2	47.2		63.8	43.4
TiO_2	0.5		0.6	0.8
Al_2O_3	7.2		15.0	6.3
Fe_2O_3	2.7		2.5	2.9
Cr_2O_3	0.1		0.03	0.5
FeO	15.5		8.4	9.3
MnO	0.2		0.04	0.2
MgO	12.0		1.6	25.3
NiO	0.1		0.01	0.2
CoO	0.01		0.003	0.01
CaO	11.6		2.0	10.4
Na_2O	1.2		3.1	0.1
K_2O	0.6		1.9	0.02
P_2O_5	0.04		0.1	0.04
H_2O	1.0		1.0	0.5
Sc	43		14	28
V	258		143	314
Rb	27		80	3
Sr	109		252	75
La	5		27	1
Ce	11		51	3
Nd	8		23	3
Sm	2		4	1
Eu	1		1	0.4
Tb	0.4		0.5	0.3
Ho	0.5		1	0.3
Lu	0.2		0.2	0.1
Hf	2		5	1
Th	1		8	0.1
	FC: Melt	Wall rock	AFC: Melt	
Pressure (MPa)	400	400	400	
Mass (m.u.)	100	300		75
Decrement, ΔT(°C)	20		20	
Initial wall-rock T (°C)		650		
Initial recharge T (°C)				1600
Recharge trigger T(°C)				1050
FmZero		0.05		

The parental melt is initialised with the CM (i.e. sample 199 610), the wall rock is the average arenites and the komatiite from Sarah Jane Barnes & Often (1990) recharge magma.

All oxides are reported in wt%, and all trace elements are reported in ppm.

similar to the CM, the concentrations do not entirely overlap. We note that K, Ti, Cr, Mn, Fe, Co and Ni concentrations of the model melt are calculated based on the mineral end-member thermodynamic components specified in rhyolite–MELTS (v.1.2.x; Ghiorso & Gualda, 2015, Gualda *et al*., 2012) and not by selecting temperature-independent partition coefficients.

Stage 2 (400 MPa)

Supplement 10 shows a model overview with the resulting cumulate stratigraphy. Figure 14 shows the major element compositions of the modelled liquid line of descent together with the modelled incremental bulk cumulates, and Fig. 15 shows the primitive mantle-normalised model result together with model members and evolved mafic samples.

Initiation of the model is with a liquidus temperature of $T^M{}_0 \sim 1273°C$, crystallising clinopyroxene, olivine and minor spinel as it cools. When the melt has cooled to c. 1150°C, the wall-rock melt fraction passes the percolation threshold and releases 9.2 m.u. of anatectic melt to the magma chamber, increasing the saturation of spinel.

When the magma chamber has cooled to 1050°C, a recharge event is triggered, adding 75 m.u. of primitive komatiitic melt (i.e. $\bar{x}$) to the chamber. The heat supplied by the recharged liquid increases the chamber temperature to 1333°C, which provides more heat to the wall rock. When the magma again cools to a temperature of

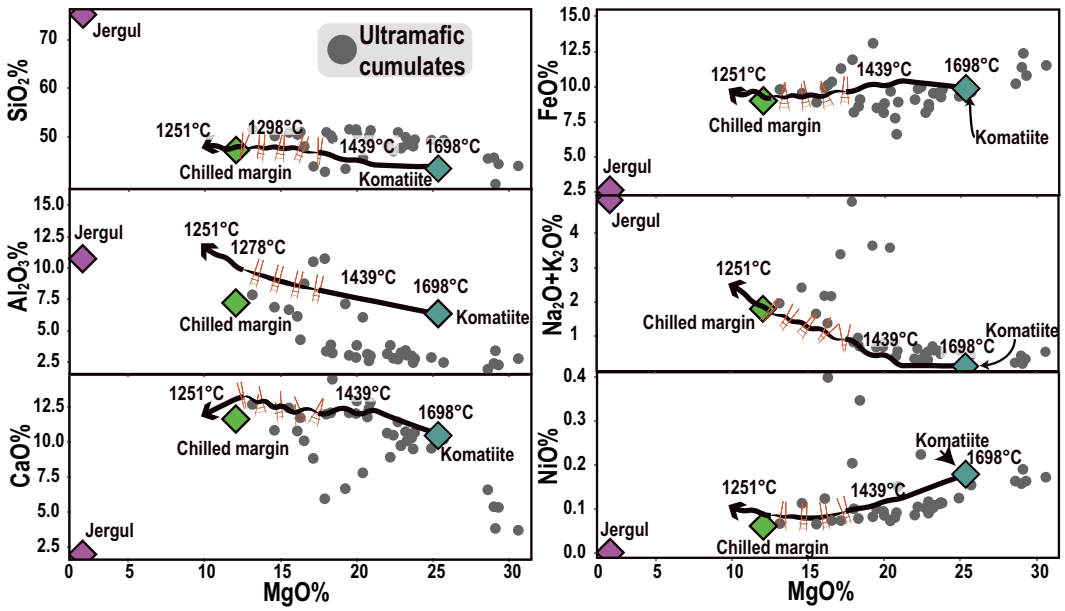

Fig. 12. Results from the MCS–PhaseEQ 700 MPa AFC simulation presented as wt% oxide Fenner diagrams. The black line represents the liquid line of descent that starts at the assumed komatiitic parental melt and evolves towards lower MgO concentrations. The orange ticked section (12–18 wt% MgO; 1298–1410 T^{M}(°C)) represents the range that has compositions comparable to the CM of the Gallujavri intrusion (cf. sample 199 610). Figure 13 presents normalised trace elements from this section.

1167°C, it has digested c. 48 m.u. of the wall rock and orthopyroxene crystallises together with spinel.

From 1143°C to when the system reaches thermal equilibrium at c. 1005°C, orthopyroxene, clinopyroxene and spinel co-precipitate. At thermal equilibrium, the magma in the chamber (i.e. M + R) has assimilated c. 79 m.u. of wall rock. The continued FC of the liquid leads to saturation of plagioclase at c. 947°C, rhombohedral (Rhm)-oxides (ilmenite) at c. 897°C and biotite at 727°C.

As demonstrated in the Fenner diagrams in Fig. 14, the liquid line of descent shows suitable matches with the mafic samples for SiO_2, CaO and the alkalis ($Na_2O + K_2O$) for comparable MgO concentrations. In the Al_2O_3 diagram, the mafic samples correlate better with the modelled liquid after the recharge event. The NiO liquid line of descent flattens out both for the initial magma and the recharged hybrid at a higher concentration than the whole-rock mafic samples and dolerites. The premature termination of crystallising olivine in the model could explain this feature or that MELTS does not include any Ni-sulphide phases. Stage 2 cumulates (pink in Fig. 14) show a good correlation in all the plots; one exception is that the simulations do not stabilise a significant potassium-bearing phase.

There is general agreement between the highlighted MCS liquid in Fig. 14 and the primitive mantle-normalised trace elements in Fig. 15. In Fig. 15a, there are similar patterns between the whole-rock evolved mafic samples and the MCS liquid. There are some differences, notably too low Sr and Ti in the MCS liquid.

The REEs in Fig. 15b have similar fractionation trends in both the MCS liquid and the whole-rock mafic samples, but with slight relative depletion of Sm and Eu in the MCS liquid. The minor positive europium anomaly exhibited by the mafic samples might be an effect of plagioclase accumulation. In Fig. 15c, the patterns are similar in the transition metal plot, but the gabbros are more depleted in Sc, Cr, Mn, Fe, Co and Ni and more enriched in Ti and V relative to the MCS liquid.

Mineral chemistry (stages 1 and 2)

Figures 16 and 17 show the modelled MCS mineral chemistries with mineral EPMA data. In Fig. 16, olivine, clinopyroxene, orthopyroxene and feldspar are presented graphically as Harker diagrams. Figure 17 presents the spinels and Rhm-oxides (i.e. ilmenite) in a TiO_2–FeO–Fe_2O_3 ternary diagram (Fig. 17a) and the spinels in Fe^{3+}–Cr–Al ternary and TiO_2 vs xFe^{3+} binary diagrams (Fig. 17b, c). In all the figures, grey symbols represent model compositions at 700 MPa (stage 1) and black symbols at 400 MPa (stage 2).

In the Harker diagrams in Fig. 16, the MCS phases replicate the observed major element compositions. The Fo content of the most primitive olivine crystallised at 700 MPa is 93% and terminates when the liquid reaches 1354°C, with Fo_{90}. The MCS pyroxenes show a good overlap with the major element data. In the TiO_2-diagram, the modelled clinopyroxene compositions are close but only touch the observed trend. In the model, only feldspar crystallised in stage 2, after thermal equilibrium with the wall rock. The modelled feldspar compositions overlap well with Al_2O_3, CaO and Na_2O of the most primitive plagioclase data but with a slight relative enrichment in K_2O (not shown in Fig. 16).

The first spinels in both the 700 and 400 MPa cases start as Al-chromite, overlapping with our EPMA data (Fig. 17a, b). Not represented in our spinel data is the subsequent evolution along the ulvöspinel–magnetite tie-line (Fig. 17a). Our measured ilmenite mineral chemistry is comparable to the modelled Rhm-oxide MELTS phase, plotting close to the ilmenite end-member in Fig. 17a. Plots with the compositional fields of Barnes & Roeder (2001) show a similar Fe–Ti trend commonly developed by chromite crystallised from parental komatiitic melts (Fig. 17b, c). However, in Fig. 17b, the modelled spinel composition diverges and crosses the empirical spinel gap for chromite in mafic and ultramafic rocks (Barnes & Roeder, 2001). This divergence is interpreted as a combination of Al loss with metamorphism (Barnes & Roeder, 2001) and a MELTS spinel thermodynamic calibration that is slightly off.

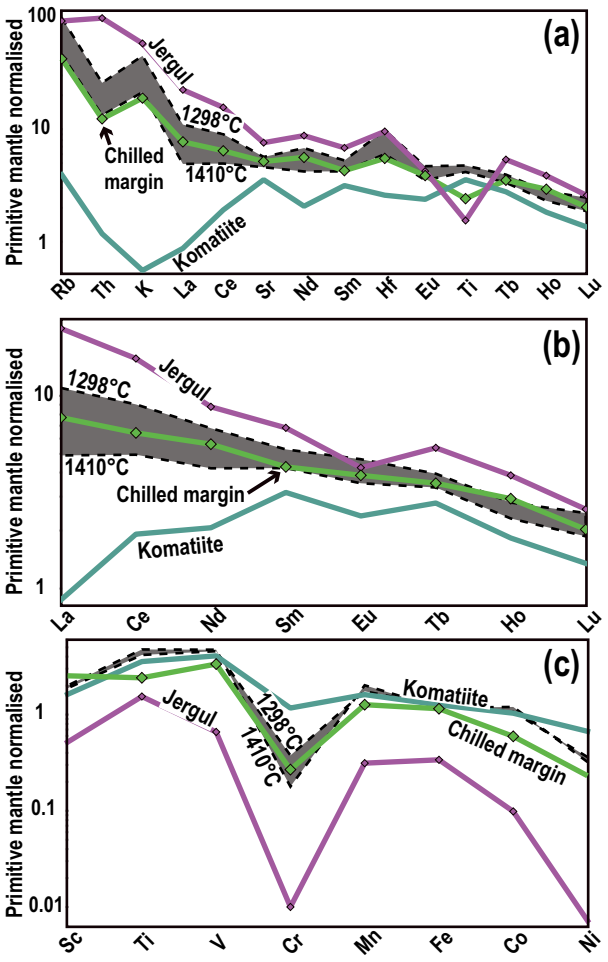

Fig. 13. The MCS–PhaseEQ 700 MPa AFC simulated liquid for the temperature range 1298–1410°C (grey field; cf. orange ticked line in Fig. 12), together with the assumed parental komatiite, Jergul Complex wall rock and Gallujavri CM. (a) Multi-element primitive mantle-normalised diagram (Sun & McDonough, 1989). (b) REE primitive mantle-normalised diagram (Sun & McDonough, 1989). (c) Transition metals primitive mantle-normalised diagram (Jagoutz *et al.*, 1979).

Implications for petrogenesis

With our defined assumptions, the overall petrological evolution of the Gallujavri intrusion replicates well with a polybaric, parental komatiite, RAFC model, which corroborates our thermobarometric data. The chemical features, such as LILE enrichment, can be explained by crustal contamination. There is, however, uncertainty as to at what crustal level the contamination occurred. The arenitic host of the Gallujavri intrusion consists of material likely derived from the Jergul Complex, giving them similar chemical features, especially regarding the LILE elements (Fig. 10a), thus identifying one or the other as the main contaminant is difficult.

The model indicates that the Gallujavri intrusion represents an open magmatic system requiring at least one recharge event to stabilise orthopyroxene at 400 MPa. There is some ambiguity as to the number and composition of the recharge(s). Based on our polybaric model, we can envision a range of possible magma-evolution scenarios. For example, the composition of the recharging melt could range from undifferentiated primitive to differentiated anywhere in the section between 400 MPa and the mantle source, or a combination. The modelling, however, shows that the recharging melt must be considerably different from the stage-2 starting composition to alter the modelled evolution trend substantially from pure FC. We chose a primitive 'undifferentiated' komatiitic melt as the recharging liquid, as at stage 2, the starting hybrid melt (i.e. CM) has diverged enough from the starting komatiite to uphold the criteria of being compositionally different.

Figure 18 summarises some of the key aspects of our petrogenetic model and is well in line with an emerging consensus of trans-crustal magma plumbing systems (Hildreth & Moorbath, 1988; Annen *et al.*, 2006; Cashman *et al.*, 2017; Ganne *et al.*, 2018; Magee *et al.*, 2018; Gualda *et al.*, 2019). Recent advances in geophysical techniques provide exciting insights into trans-crustal magma systems (Magee *et al.*, 2018). For example, in the 60-km-long Yellowstone caldera, USA, tomographic studies have imaged a large (c. 10^4 km^3) low-velocity body, 5–17 km deep and a c. 4.5 times larger lower-crustal body that acts as a link between the Yellowstone mantle plume and the shallower body (Farrell *et al.*, 2014; Huang *et al.*, 2015; Cashman *et al.*, 2017).

In our model, primitive melt first intrudes the lower crust where it perturbs the geothermal gradient creating a deep-crustal hot zone similar to models for arc environments (Annen *et al.*, 2006). When the surrounding crust exceeds the solidus, it begins to undergo partial melting, creating a hybrid melt that combines residual melts from the crystallisation of the komatiite and anatectic crustal melt. As in our model, the geothermal gradient or any localised thermal profile resulting from preceding injections would control the relative contribution of the different sources to the hybrid melt (Annen *et al.*, 2006).

In the second stage, the hybrid melt segregates from the lower-crustal reservoir and migrates to shallower crustal levels (Fig. 18). If the deeper reservoir has attained a mushy state (i.e. a system of interconnected crystals in a melt matrix), segregation requires porous media processes (Cashman *et al.*, 2017). Another possibility is that crystal segregation creates a strongly physically differentiated reservoir, resulting in a crystal poor and buoyant layer of hybrid melt (Annen *et al.*, 2006).

Once the hybrid melt intrudes the middle crust, the processes mirror those of the staging chamber (Fig. 18). The shallow chamber requires higher magma input rates to remain above the solidus as the ambient temperatures are lower (Annen *et al.*, 2006; Cashman *et al.*, 2017). To counteract this, our model proposes pre-heating the middle crust to maintain a molten Gallujavri chamber. However, the thermal requirement for maintaining middle-crustal non-eruptive crystal mushes, as opposed to a melt-rich magma chamber, are smaller (Cashman *et al.*, 2017).

The last stage in the petrogenesis of the Gallujavri intrusion is the recharge of primitive, uncontaminated komatiite. It may seem counterintuitive that melt passing through the same system should not be similarly affected by fractionation and assimilation; however, many Archaean greenstones and post-Archaean flood-basalt provinces exhibit komatiite or picrite flows cogenetic with fractionated basalts (Lister *et al.*, 1991). Furthermore, in our case, the coeval to slightly younger primitive extrusive komatiites within the KCLGB are suggestive of such a process. A possible explanation is the formation of a thermo-chemical insulator surrounding the lower- to mid-crustal plumbing system (Larsen *et al.*, 2018). For example, in the Reinfjord Ultramafic Complex, Seiland Igneous Province, Norway (Larsen *et al.*, 2018; Grant *et al.*, 2020), Grant *et al.* (2016) documented a reverse fractionation sequence whereby cumulates

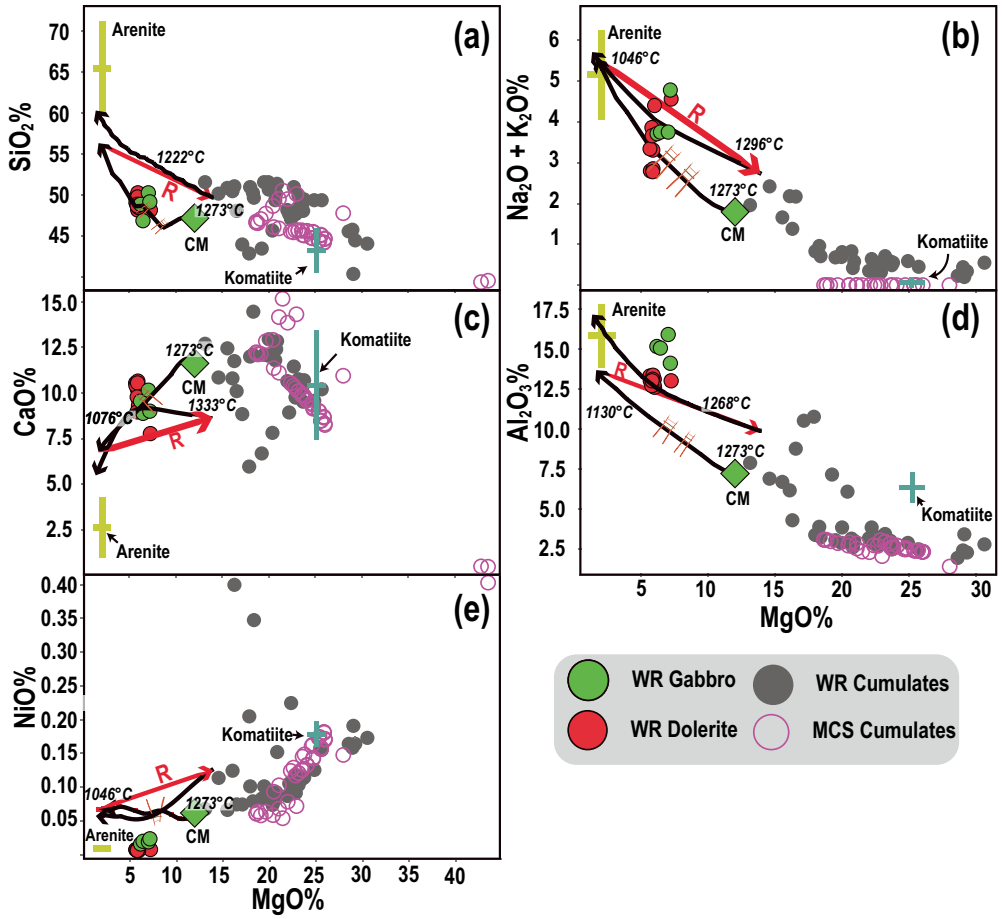

Fig. 14. Results from the MCS–PhaseEQ 400 MPa RAFC simulation presented as wt% oxide Fenner diagrams. The black line represents the liquid line of descent that starts at the composition of the CM and evolves towards lower MgO concentrations. The orange ticked section (6–9 wt% MgO; 1130–1193 T^{M}(°C)) represents the range that has compositions comparable to the evolved mafic samples that are assumed to approach liquid compositions. Figure 15 presents normalised trace elements from this section. The red vector labelled R indicates the **R**echarge event adding 75 m.u. of komatiitic melt to the system.

became progressively more MgO and olivine rich with time. This reverse trend was interpreted as resulting from contamination of the intrusion by the host gabbro-norite, evident in the marginal zones but limited in the central parts of the complex (Grant *et al.*, 2016; Grant *et al.*, 2020).

Our proposed multistage petrogenetic model for the Gallujavri intrusion does not serve as a unique example in the KCLGB, and similar models have been proposed for various ultramafic–mafic layered intrusions throughout its c. 400 Ma magmatic history. For example, our model resembles the petrogenetic model for the c. 2.44 Ga Akanvaara and Koitelainen mafic layered intrusions in northern Finland (Hanski *et al.*, 2001b; Hanski & Huhma, 2005). Hanski *et al.* (2001b) determined the Os isotopic compositions at different stratigraphic positions in the intrusions and found near-chondritic ratios with only slight variation and no systematic differences relative to stratigraphic position. Combined with Nd isotope systematics, Hanski *et al.* (2001b) proposed a model of deep-crustal assimilation (15%–25%), coupled with minor *in situ* assimilation of country-rock material.

Another example is the contemporary Kevitsa Complex (c. 2.06 Ga; Mutanen & Huhma, 2001). Here, Luolavirta (2018) proposed a multistage model with many parallels to the Gallujavri intrusion. The spatially confined but markedly different drill core lithological and compositional profiles inside and outside the Kevitsa ore domain led Luolavirta *et al.* (2018a) to suggest a model of multiple injections. During the first stage, the central dunite formed by accumulation in a picritic magma conduit; in the second stage, evolved basaltic liquid (fractionated at depth from the initial picritic melt) intruded through the same plumbing system (Luolavirta *et al.*, 2018a; Luolavirta *et al.*, 2018b). The third stage defines repeated injections of basaltic magma into the dynamically open, hot interior of the intrusion (Luolavirta *et al.*, 2018a; Luolavirta *et al.*, 2018b).

The polybaric and multistage model presented here is probably widely applicable to the petrogenesis of Palaeoproterozoic Fennoscandian (ultra)mafic intrusions and also a potentially effective mechanism for forming viable economic PGE Ni–Cu deposits. For example, the Ni–PGE ores of the Kevitsa intrusion, with a Ni tenor of 6%–60% (Luolavirta *et al.*, 2018b) and tens of ppm PGE (Maier & Groves, 2011), is believed to be the result of cannibalisation (assimilation) of proto-ores deposited in stage 2 by the repeated magma injections in stage 3 (Luolavirta, 2018). Thus, identifying this process using MCS modelling may be an important prospecting tool.

Although our hypothesis shows many petrogenetic similarities to many of the ore-hosting mafic–ultramafic intrusions of the

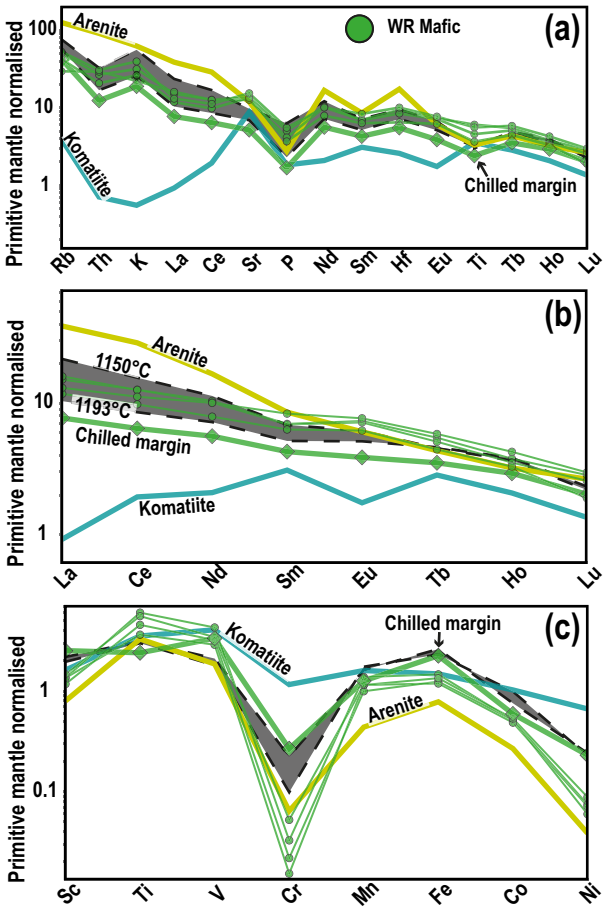

Fig. 15. The MCS–PhaseEQ 400 MPa RAFC simulated liquid for the temperature range 1130°C–1193°C (grey field; cf. orange ticked line in Fig. 14), together with evolved gabbroic samples that are assumed to approach liquid compositions (green circles), the arenite host rock, komatiite recharge and the starting liquid (i.e. CM). (a) Multi-element primitive mantle-normalised diagram (Sun & McDonough, 1989). (b) REE primitive mantle-normalised diagram (Sun & McDonough, 1989). (c) Transition metals primitive mantle-normalised diagram (Jagoutz *et al.*, 1979).

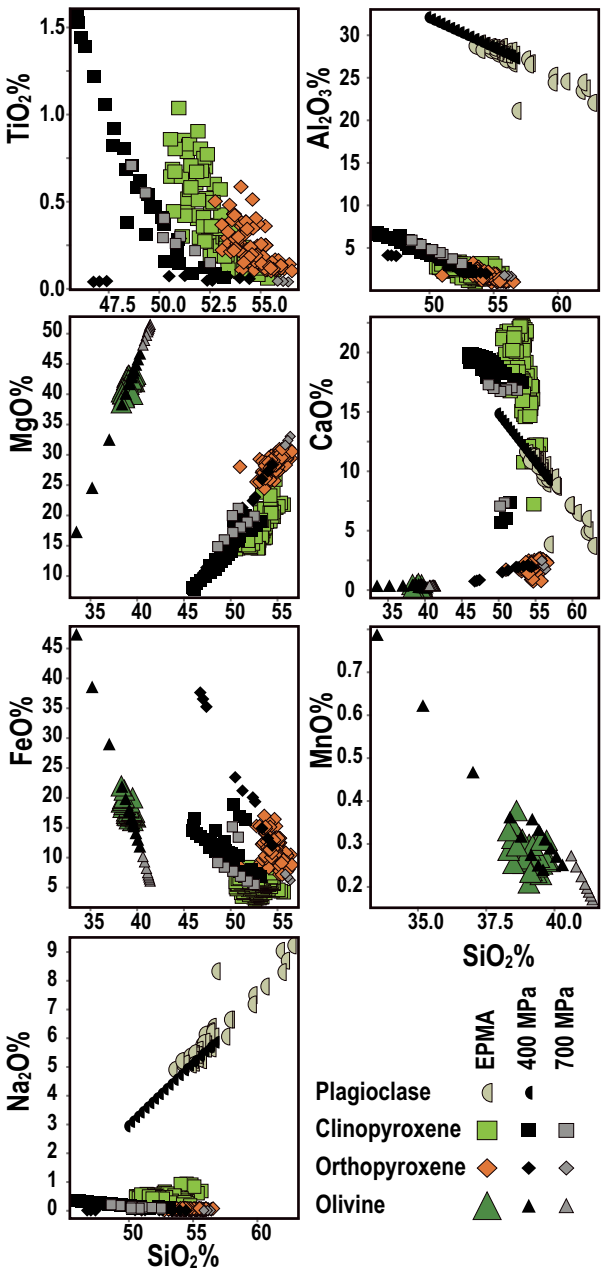

Fig. 16. Harker-type diagrams showing MCS–PhaseEQ mineral phase compositions for the 700 MPa AFC (grey) and 400 MPa RAFC (black) simulations. EPMA data are presented in colours.

Fennoscandian Shield, the size of the Gallujavri intrusion may be too small for hosting an economically viable ore (Nilsson & Often, 2009). Furthermore, there is no discernible correlation between NiO and MgO in our olivine data. These Ni contents are relatively high when considering the low Fo content and are inconsistent with crystallisation from a sulphur-saturated or Ni-depleted melt (Brenan & Caciagli, 2000). This interpretation is supported by the whole-rock NiO vs MgO (Fig. 9d), with the observed linear trends being inconsistent with a sulphur-saturated system in which immiscible sulphide melt scavenges Ni from the silicate melt. Another possibility is that if an immiscible sulphide liquid existed, restricted interaction with the silicate liquid would lower apparent sulphide–silicate liquid partition coefficients (i.e. low R-values; Campbell & Naldrett, 1979). On the other hand, both adjacent and remote intrusions of the same type as Gallujavri are poorly investigated (Nilsson & Often, 2009) and therefore represent attractive targets for further investigations into the petrogenesis and ore potential of the Palaeoproterozoic komatiitic magmatism in the KGB.

CONCLUSIONS

Uniform signs of crustal assimilation characterise the studied ultramafic Gallujavri intrusion. Combining the features of assimilation with the genetic indications of the spinel compositions, the polybaric thermobarometry and the spatial and temporal association with ultramafic volcanic rocks suggest that the Gallujavri intrusion is subvolcanic.

Based on previous geochronology and our modelling results, the parental magma of the intrusion is the Ti-rich Karasjok-type komatiite observed at various places within the Fennoscandian Shield. The komatiite intruded the Archaean lower crust (c. 700 MPa, depth of

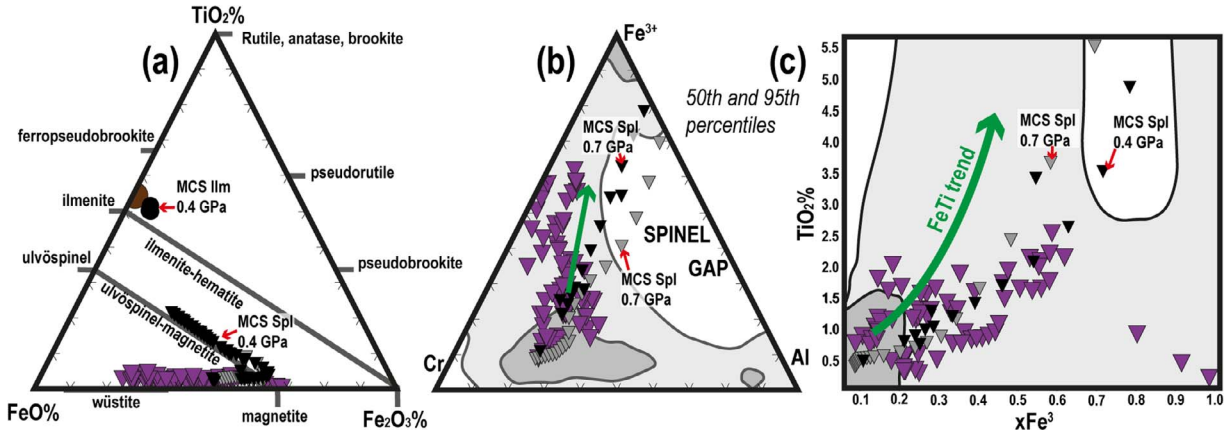

Fig. 17. Fe–Ti oxide mineral diagrams showing MCS–PhaseEQ mineral phase compositions for the 700 MPa AFC (grey) and 400 MPa RAFC (black) simulations. EPMA data are presented in colours. The contoured compositional fields and Fe–Ti trend (green arrow) in (b) & (c) from Barnes & Roeder (2001). (a) TiO_2–FeO–Fe_2O_3 ternary diagram showing the composition of the Fe–Ti oxides and the simulated phases. (b) Fe^{3+}–Cr–Al ternary diagram relating spinel compositions to the simulated phases. (c) TiO2 vs xFe^{3+} ($Fe^{3+}/(Cr + Al + Fe^{3+})$) diagram for spinel and simulated phases.

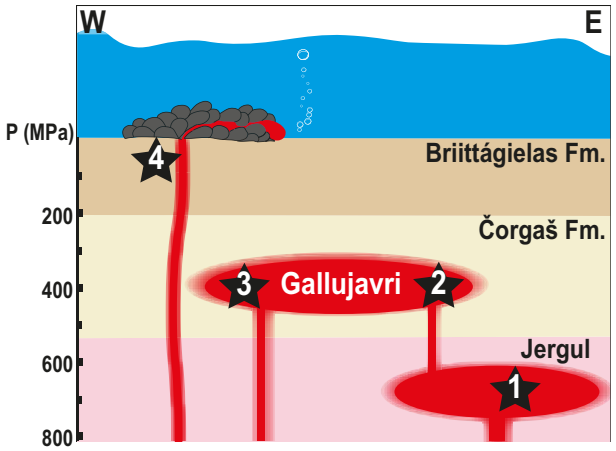

Fig. 18. Conceptual model illustrating a hypothesised trans-crustal magma plumbing system. Step 1: The dense komatiitic magma intrudes and stalls in the lower crust where the ambient temperature is high. Partial igneous differentiation occurs as the intruding melt heats the country rocks, assimilating anatectic melt of gneissic granodiorite and fractionating out solids. Step 2: The hybrid magma, expelled either by mush compaction or buoyancy, ascends to higher levels in the crust, leaving behind refractory cumulate rocks. The influx of heat pushes the host rock over the solidus, incorporating siliceous anatectic melt and fractionating out solids. Step 3: Recharge of primitive komatiite, either through the pre-established feeder or through intersecting dykes, stabilises orthopyroxene. Step 4: Trans-crustal dykes supply extrusive pillowed komatiite with little or no interaction with the crust.

c. 25 km), where fractionation and assimilation resulted in a hybrid melt consistent with the composition observed in the Gallujavri CM. Replication of our thermobarometric estimates and petrographic observations requires a second stage of recharge, assimilation and fractionation at middle crustal levels (c. 400 MPa, depth of c. 15 km).

Our modelling suggests that the Gallujavri intrusion is part of a complex and vertically extensive magmatic structure with many similarities to other Fennoscandian ultramafic–mafic layered intrusions. We interpret the Gallujavri intrusion to represent a Palaeoproterozoic example of a trans-crustal magmatic system, as defined by geophysical imaging of active magmatic plumbing structures elsewhere.

FUNDING

This study is a part of Alf Andre Orvik's PhD project on the Gallujavri intrusion in the Karasjok Greenstone Belt, funded by the Department of Geoscience and Petroleum, Faculty of Engineering, at the NTNU and the Geological Survey of Norway.

DATA AVAILABILITY STATEMENT

The data underlying this article are available in the article and in its online supplementary material.

ACKNOWLEDGEMENTS

We are thankful for the thoughtful reviews by Wolfgang Maier, Ville Järvinen and Wendy Bohrson. We acknowledge the past drilling program by Tertiary Gold Ltd., which is a prerequisite for this study. We further acknowledge Store Norske Gull AS for providing access to the company's geochemical assays and in-tray XRD scans. We are grateful to Kristian Drivenes, the operator of the microprobe at NTNU. We also want to acknowledge Øyvind Skaar at the Geological Survey of Norway for his help with the LA–ICP–MS analysis.

REFERENCES

Annen, C., Blundy, J. D. & Sparks, R. S. J. (2006). The genesis of intermediate and silicic magmas in deep crustal hot zones. *Journal of Petrology* **47**, 505–539.

Arndt, N., Ginibre, C., Chauvel, C., Albarède, F., Cheadle, M., Herzberg, C., Jenner, G., Lahaye, F. (1998). Were komatiites wet? *Geology* **26**, 739–742.

Ashchepkov, I. V., Pokhilenko, N. P., Vladykin, N. V., Rotman, A. Y., Afanasiev, V. P., Logvinova, A. M., Kostrovitsky, S. I., Pokhilenko, L. N., Karpenko, M. A., Kuligin, S. S., Malygina, E. V., Stegnitsky, Y. B., Alymova, N. A. & Khmelnikova, O. S. (2008) *Reconstruction of Mantle Sections Beneath Yakutian Kimberlite Pipes Using Monomineral Thermobarometry*. London: Geological Society of London, Special Publication, pp.335–352.

Ballhaus, C., Berry, R. F. & Green, D. H. (1990). Oxygen fugacity controls in the Earth's upper mantle. *Nature* 437–440.

Barnes, S.-J. (1985). The petrography and geochemistry of komatiite flows from the Abitibi Greenstone Belt and a model for their formation. *Lithos* **18**, 241–270.

Barnes, S. J. & Often, M. (1990). Ti-rich komatiites from Northern Norway. *Contributions to Mineralogy and Petrology* **105**, 42–54.

Barnes, S. J. & Roeder, P. L. (2001). The range of spinel compositions in terrestrial mafic and ultramafic rocks. *Journal of Petrology* **42**, 2279–2302.

Barsdell, M. (1988). Petrology and petrogenesis of clinopyroxene-rich tholeiitic lavas, Merelava volcano, Vanuatu. *Journal of Petrology* **29**, 927–964.

Beswick, A. (1982) Some geochemical aspects of alteration and genetic relations in komatiitic suites. In: (Arndt N. & Nisbet E. (eds)) *Komatiites*. London: Allen, pp.283–308.

Bingen, B., Solli, A., Viola, G., Torgersen, E., Sandstad, J. S., Whitehouse, M. J., Røhr, T. S., Ganerød, M. & Nasuti, A. (2015). Geochronology of the palaeoproterozoic kautokeino greenstone belt, Finnmark, Norway: tectonic implications in a fennoscandia context. *Norsk Geologisk Tidsskrift* **95**, 365–396.

Birner, S. K., Cottrell, E., Warren, J. M., Kelley, K. A. & Davis, F. A. (2018). Peridotites and basalts reveal broad congruence between two independent records of mantle fO2 despite local redox heterogeneity. *Earth and Planetary Science Letters* **494**, 172–189.

Blundy, J., Cashman, K. V. & Berlo, K. (2008). Evolving magma storage conditions beneath Mount St. Helens inferred from chemical variations in melt inclusions from the 1980–1986 and current (2004–2006) eruptions. US Geological Survey.

Boettcher, A., Mysen, B. O. & Modreski, P. J. (1975). Melting in the mantle: phase relationships in natural and synthetic peridotite–H2O and peridotite–H2O–CO2 systems at high pressures. In: Ahrens, L. H., Dawson, J. B., Duncan, A. R. & Erlank, A. J. (eds.) Physics and Chemistry of the Earth: Pergamon, 855–867.

Bohrson, W. A., Spera, F. J., Ghiorso, M. S., Brown, G. A., Creamer, J. B. & Mayfield, A. (2014). Thermodynamic model for energy-constrained open-system evolution of crustal magma bodies undergoing simultaneous recharge, assimilation and crystallization: the magma chamber simulator. *Journal of Petrology* **55**,1685–1717.

Bohrson, W. A., Spera, F. J., Heinonen, J. S., Brown, G. A., Scruggs, M. A., Adams, J. V., Takach, M. K., Zeff, G. & Suikkanen, E. (2020). Diagnosing open-system magmatic processes using the magma chamber simulator (MCS): part I—major elements and phase equilibria. *Contributions to Mineralogy and Petrology* **175**, 1–29.

Boyd, R., Bjerkgård, T., Nordahl, B. & Schiellerup, H. (2016) Mineral resources in the Arctic. Geological Survey of Norway.

Braathen, A. & Davidsen, B. (2000). Structure and stratigraphy of the Palaeoproterozoic Karasjok Greenstone Belt, North Norway - regional implications. *Norsk Geologisk Tidsskrift* **80**, 33–50.

Bradley, J. (2003) Finnmark Project, Diamond Drill Program - April 2003. In: *Summary and review*. Norwegian Directorate of Mining: Tertiary Gold Limited, p.14.

Brenan, J. M. & Caciagli, N. C. (2000). Fe-Ni exchange between olivine and sulphide liquid: implications for oxygen barometry in sulphide-saturated magmas. *Geochimica et Cosmochimica Acta* **64**, 307–320.

Brey, G. P. & Köhler, T. (1990). Geothermobarometry in four-phase lherzolites II. New thermobarometers, and practical assessment of existing thermobarometers. *Journal of Petrology* **31**(6), 1353–1378.

Burns, R. G. & Brown, G. E., Jr. (1982) Chapter 11. Olivines and silicate spinels. In: (Roger G. B. (ed)) *Orthosilicates*. De Gruyter, pp. 275–382.

Campbell, I. & Naldrett, A. (1979). The influence of silicate: sulfide ratios on the geochemistry of magmatic sulfides. *Economic Geology* **74**, 1503–1506.

Cashman, K. V., Sparks, R. S. J. & Blundy, J. D. (2017). Vertically extensive and unstable magmatic systems: a unified view of igneous processes. *Science* 355, eaag3055.

Cottrell, E., Birner, S., Brounce, M., Davis, F., Waters, L. & Kelley, K. (2021). Oxygen Fugacity Across Tectonic Settings. *AGU Geophysical Monograph*. In Magma Redox Geochemistry (eds R. Moretti and D.R. Neuville).

Deer, W. A.,. F. R. S., Howie, R. A. & Zussman, J. (2013) Spinel group. In: *An Introduction to the Rock-Forming Minerals*. Mineralogical Society of Great Britain and Ireland.

Duncan, R. A., Hooper, P. R., Rehacek, J., Marsh, J. S. & Duncan, A. R. (1997). The timing and duration of the Karoo igneous event, southern Gondwana. *Journal of Geophysical Research-Solid Earth* **102**, 18127–18138.

Erns, R. E. & Jowitt, S.M. (2013). Large igneous provinces (LIPs) and metallogeny. *Society of Economic Geologists Special Publication* **17**, 17–51.

Farrell, J., Smith, R. B., Husen, S. & Diehl, T. (2014). Tomography from 26 years of seismicity revealing that the spatial extent of the Yellowstone crustal magma reservoir extends well beyond the Yellowstone caldera. *Geophysical Research Letters* **41**, 3068–3073.

Frey, F. A. & Green, D. H. (1974) The mineralogy, geochemistry and origin of Iherzolite inclusions in Victorian basanites. *Geochimica et Cosmochimica Acta* **38**, 1023–1059.

Frost, B. R. (1991) Introduction to oxygen fugacity and its petrologic importance. *Reviews in Mineralogy and Geochemistry* **25**, 1–9.

Frost, D. J. & McCammon, C. A. (2008). The redox state of Earth's mantle. *Annual Review of Earth and Planetary Sciences* **36**, 389–420.

Ganne, J., Bachmann, O. & Feng, X. (2018). Deep into magma plumbing systems: interrogating the crystal cargo of volcanic deposits. *Geology* **46**, 415–418.

Ghiorso, M. S. & Gualda, G. A. R. (2015) An H2O–CO2 mixed fluid saturation model compatible with rhyolite-MELTS. In: *Contributions to Mineralogy and Petrology*. Springer, p.53.

Ghiorso, M. S., Hirschmann, M. M., Reiners, P. W. & Kress, V. C. (2002). The pMELTS: a revision of MELTS for improved calculation of phase relations and major element partitioning related to partial melting of the mantle to 3 GPa. *Geochemistry, Geophysics, Geosystems* **3**, 1–35.

Ghiorso, M. S. & Sack, R. O. (1995). Chemical mass transfer in magmatic processes IV. A revised and internally consistent thermodynamic model for the interpolation and extrapolation of liquid-solid equilibria in magmatic systems at elevated temperatures and pressures. *Contributions to Mineralogy and Petrology* **119**, 197–212.

Grant, T. B., Larsen, R. B., Anker-Rasch, L., Grannes, K. R., Iljina, M., McEnroe, S., Nikolaisen, E., Schanche, M. & Øen, E. (2016). Anatomy of a deep crustal volcanic conduit system; the Reinfjord ultramafic complex, Seiland Igneous Province, Northern Norway. *Lithos* **252–253**, 200–215.

Grant, T. B., Larsen, R. B., Brown, E. L., Müller, A. B. & McEnroe, S. (2020). Mixing of heterogeneous, high-MgO, plume-derived magmas at the base of the crust in the Central Iapetus Magmatic Province (ma 610-550): origin of parental magmas to a global LIP event. *Lithos* **364–365**, 105535.

Gualda, G. A. R. & Ghiorso, M. S. (2015). MELTS_Excel: A Microsoft Excel-based MELTS interface for research and teaching of magma properties and evolution. *Geochemistry, Geophysics, Geosystems* **16**, 315–324.

Gualda, G. A. R., Ghiorso, M. S., Lemons, R. V. & Carley, T. L. (2012). Rhyolite-MELTS: a modified calibration of MELTS optimized for silica-rich, fluid-bearing magmatic systems. *Journal of Petrology* **53**, 875–890.

Gualda, G. A. R., Gravley, D. M., Deering, C. D. & Ghiorso, M. S. (2019). Magma extraction pressures and the architecture of volcanic plumbing systems. *Earth and Planetary Science Letters* **522**, 118–124.

Hansen, H., Slagstad, T. & Bergh, S. G. (2020). Geochemical volcanostratigrapy defines the tectonic evolution of the Karasjok Greenstone Belt, Finmark. *The 34th Nordic Geological Winter Meeting, Oslo* .

Hanski, E. & Huhma, H. (2005) *Chapter 4 Central Lapland greenstone belt*. In: Lehtinen, M., Nurmi, P. A. & Rämö, O. T. (eds.) Precambrian Geology of Finland Key to the Evolution of the Fennoscandian Shield: Elsevier, pp. 139–193.

Hanski, E., Huhma, H., Rastas, P. & Kamenetsky, V. S. (2001a). The palaeoproterozoic komatiite-picrite association of Finnish Lapland. *Journal of Petrology* **42**, 855–876.

Hanski, E., Walker, R., Huhma, H. & Suominen, I. (2001b). The Os and Nd isotopic systematics of c. 2.44 Ga Akanvaara and Koitelainen mafic layered intrusions in northern Finland. *Precambrian Research* **109**, 73–102.

Hawthorne, F. C., Oberti, R., Harlow, G. E., Maresch, W. V., Martin, R. F., Schumacher, J. C. & Welch, M. D. (2012). Nomenclature of the amphibole supergroup. *American Mineralogist* **97**, 2031–2048.

Heggie, G. J., Barnes, S. J. & Fiorentini, M. L. (2013). Application of lithogeochemistry in the assessment of nickel-sulphide potential in komatiite belts from northern Finland and Norway. *Bulletin of the Geological Society of Finland* **85**, 107–126.

Heinonen, J. S., Bohrson, W. A., Spera, F. J., Brown, G. A., Scruggs, M. A. & Adams, J. V. (2020) Diagnosing open-system magmatic processes using

the magma chamber simulator (MCS): part II—trace elements and isotopes. In: *Contributions to Mineralogy and Petrology*. Berlin, Heidelberg: Springer, pp. 1–21.

Heinonen, J. S., Iles, K. A., Heinonen, A., Fred, R., Virtanen, V. J., Bohrson, A., Spera, F. J., Bohrson, W. A. & Spera, F. J. (2021) From Binary Mixing to Magma Chamber Simulator. In Crustal Magmatic System Evolution (eds M. Masotta, C. Beier and S. Mollo).

Heinonen, J. S., Luttinen, A. V., Spera, F. J. & Bohrson, W. A. (2019). Deep open storage and shallow closed transport system for a continental flood basalt sequence revealed with magma chamber simulator. *Contributions to Mineralogy and Petrology* **174**, 87–87.

Hildreth, W. & Moorbath, S. (1988). Crustal contributions to arc magmatism in the Andes of Central Chile. *Contributions to Mineralogy and Petrology* **98**, 455–489.

Hirschmann, M. M. (2000). Mantle solidus: experimental constraints and the effects of peridotite composition. *Geochemistry, Geophysics, Geosystems* .

Huang, H. H., Lin, F. C., Schmandt, B., Farrell, J., Smith, R. B. & Tsai, V. C. (2015). The Yellowstone magmatic system from the mantle plume to the upper crust. *Science* **348**, 773–776.

Huppert, H. E. & Sparks, R. S. J. (1985). Cooling and contamination of mafic and ultramafic magmas during ascent through continental-crust. *Earth and Planetary Science Letters* **74**, 371–386.

Irvine, T. N. (1965). Chromian spinel as a petrogenetic indicator: part 1. Theory. *Canadian Journal of Earth Sciences* **2**, 648–672.

Irvine, T. N. (1967). Chromian spinel as a Petrogenetic indicator: part 2. Petrologic applications. *Canadian Journal of Earth Sciences* 71–103.

Jagoutz, E., Palme, H., Baddenhausen, H., Blum, K., Cendales, M., Dreibus, G., Spettel, B., Lorenz, V. & Wänke, H. (1979). The abundances of major, minor and trace elements in the earth's mantle as derived from primitive ultramafic nodules. *Lunar and Planetary Science Conference Proceedings* 2031–2050.

Jagoutz, O., Muntener, O., Ulmer, P., Pettke, T., Burg, J. P., Dawood, H. & Hussain, S. (2007). Petrology and mineral chemistry of lower crustal intrusions: the Chilas Complex, Kohistan (NW Pakistan). *Journal of Petrology* **48**, 1895–1953.

Koistinen, T., Stephens, M., Bogatchev, V., Nordgulen, Ø., Wennerström, M. & Korhonen, J. (2001) Geological map of the Fennoscandian Shield 1: 2 000 000. Espoo: Geological Survey of Finland, Trondheim: Geological Survey of Norway, Uppsala: Geological Survey of Sweden, Moscow: Ministry of Natural Resources of Russia.

Krill, A. G. (1985a). Rb-Sr, U-Pb and Sm-Nd isotopic dates from Precambrian rocks of Finnmark. *Norges Geologiske Undersokelse Bulletin* **403**, 37–54.

Krill, A. G. (1985b). Svecokarelian thrusting with thermal inversion in the Karasjok-Levajok area of the northern Baltic shield. *Norges Geologiske Undersokelse Bulletin* **403**, 89–101.

Larsen, R. B., Grant, T., Sørensen, B. E., Tegner, C., McEnroe, S., Pastore, Z., Fichler, C., Nikolaisen, E., Grannes, K. R., Church, N., ter Maat, G. W. & Michels, A. (2018). Portrait of a giant deep-seated magmatic conduit system: the Seiland Igneous Province. *Lithos* **296–299**, 600–622.

Lightfoot, P. C., Hawkesworth, C. J., Hergt, J., Naldrett, A. J., Gorbachev, N. S., Fedorenko, V. A. & Doherty, W. (1993). Remobilisation of the continental lithosphere by a mantle plume: major-, trace-element, and Sr-, Nd-, and Pb-isotope evidence from picritic and tholeiitic lavas of the Noril'sk District, Siberian Trap, Russia. *Contributions to Mineralogy and Petrology* **114**, 171–188.

Lister, J. R., Campbell, I. H. & Kerr, R. C. (1991). The eruption of komatiites and picrites in preference to primitive basalts. *Earth and Planetary Science Letters* **105**, 343–352.

Liu, J., Xia, Q. K., Kuritani, T., Hanski, E. & Yu, H. R. (2017). Mantle hydration and the role of water in the generation of large igneous provinces. *Nature Communications* **8**, 1824.

Ludden, J., Gélinas, L. & Trudel, P. (1982). Archean metavolcanics from the Rouyn–Noranda district, Abitibi Greenstone Belt, Quebec. 2. Mobility of trace elements and petrogenetic constraints. *Canadian Journal of Earth Sciences* **19**, 2276–2287.

Luolavirta, K. (2018). Magmatic evolution of the Kevitsa igneous complex, northern Finland, and its relation to the associated Ni-Cu-(PGE) mineralization. *Res Terrae* **68**.

Luolavirta, K., Hanski, E., Maier, W. & Santaguida, F. (2018a). Characterization and origin of dunitic rocks in the NI-CU-(PGE) sulfide ore-bearing kevitsa intrusion, northern Finland: whole-rock and mineral chemical constraints. *Bulletin of the Geological Society of Finland* **90**, 5–32.

Luolavirta, K., Hanski, E., Maier, W. & Santaguida, F. (2018b). Whole-rock and mineral compositional constraints on the magmatic evolution of the Ni-cu-(PGE) sulfide ore-bearing Kevitsa intrusion, northern Finland. *Lithos* 37–53.

Magee, C., Stevenson, C. T. E., Ebmeier, S. K., Keir, D., Hammond, J. O. S., Gottsmann, J. H., Whaler, K. A., Schofield, N., Jackson, C. A. L., Petronis, M. S., O'Driscoll, B., Morgan, J., Cruden, A., Vollgger, S. A., Dering, G., Micklethwaite, S. & Jackson, M. D. (2018). Magma plumbing systems: a geophysical perspective. *Journal of Petrology* **59**, 1217–1251.

Maier, W. D. & Groves, D. I. (2011). Temporal and spatial controls on the formation of magmatic PGE and Ni–Cu deposits. *Mineralium Deposita* **46**, 841–857.

Melezhik, V. A., Solli, A., Fallick, A. E. & Davidsen, B. (2015). Chemostratigraphic constraints on the time of deposition of carbonate rocks in the Karasjok Greenstone Belt, northern Norway. *Norwegian Journal of Geology* **95**, 299–314.

Mutanen, T. & Huhma, H. (2001). U-Pb geochronology of the Koitelainen, Akanvaara and Keivitsa layered intrusions and related rocks. Special Paper of the Geological Survey of Finland, 229–246.

Mysen, B. O. & Boettcher, A. (1976). Melting of a hydrous mantle: III. Phase relations of garnet websterite+ H2O at high pressures and temperatures. *Journal of Petrology* **17**, 1–14.

Nilsson, L. P. & Often, M. (2005). A summary report on the Ni-Cu-PGE occurrences and their host rocks in the Precambrian of Finnmark, Northern Norway. *Geological Survey of Norway Report* 2005.085 79 pp.

Often, M. (1985). The Early Proterozoic Karasjok Greenstone Belt, Norway. A preliminary description of lithology, stratigraphy and mineralization. *Norges Geologiske Undersokelse Bulletin* **403**, 75–88.

Orvik, A. A., Slagstad, T., Nilsson, L. P. & Sørensen, B. E. (n.d.) U-Pb age and Rb-Sr, Sm-Nd and Lu-Hf isotopic fingerprints of the Ni-Cu-PGE mineralised Gallujavri intrusion, northern Norway, and its relationship to other intrusions of the Central Lapland Greenstone belt. Norwegian University of Science and Technology, in preparation.

Page, P. & Barnes, S.-J. (2009). Using trace elements in chromites to constrain the origin of podiform chromitites in the thetford mines ophiolite, Quebec, Canada. *Economic Geology* **104**, 997–1018.

Perkins, D. & Vielzeuf, D. (1992). Experimental investigation of Fe-Mg distribution between olivine and clinopyroxene: implications for mixing properties of Fe-Mg in clinopyroxene and garnet-clinopyroxene thermometry. *American Mineralogist* **77**, 774–783.

Pilet, S., Hernandez, J., Bussy, F. & Sylvester, P. J. (2004). Short-term metasomatic control of Nb/Th ratios in the mantle sources of intraplate basalts. *Geology* **32**, 113–116.

Puchtel, I., Arndt, N., Hofmann, A., Haase, K., Kröner, A., Kulikov, V., Kulikova, V., Garbe-Schönberg, C.-D. & Nemchin, A. (1998). Petrology of mafic lavas within the Onega plateau, Central Karelia: evidence for 2.0 Ga plume-related continental crustal growth in the Baltic Shield. *Contributions to Mineralogy and Petrology* **130**, 134–153.

Puchtel, I. S., Haase, K. M., Hofmann, A. W., Chauvel, C., Kulikov, V. S., Garbe-Schönberg, C. D. & Nemchin, A. A. (1997). Petrology and geochemistry of crustally contaminated komatiitic basalts from the Vetreny Belt, southeastern Baltic Shield: evidence for an early Proterozoic mantle plume beneath rifted Archean continental lithosphere. *Geochimica et Cosmochimica Acta* **61**, 1205–1222.

Puchtel, I. S., Mundl-Petermeier, A., Horan, M., Hanski, E. J., Blichert-Toft, J. & Walker, R. J. (2020). Ultra-depleted 2.05 Ga komatiites of Finnish Lapland: products of grainy late accretion or core-mantle interaction? *Chemical Geology* **554**, 119801.

Putirka, K. D. (2008). Thermometers and barometers for volcanic systems. *Minerals, Inclusions and Volcanic Processes* **69**, 61–120.

Ridolfi, F., Renzulli, A. & Puerini, M. (2009). Stability and chemical equilibrium of amphibole in calc-alkaline magmas: an overview, new thermobarometric formulations and application to subduction-related volcanoes. *Contributions to Mineralogy and Petrology* **160**, 45–66.

Ridolfi, F., Zanetti, A., Renzulli, A., Perugini, D., Holtz, F. & Oberti, R. (2018). AMFORM, a new mass-based model for the calculation of the unit formula of amphiboles from electron microprobe analyses. *American Mineralogist* **103**, 1112–1125.

Shau, Y.-H., Yang, H.-Y. & Peacor, D. R. (1991). On oriented titanite and rutile inclusions in sagenitic biotite. *American Mineralogist* **76**, 1205–1217.

Siedlecka, A. (1985). Geology of Iesjav'ri-Skognavarre area, northern Finnmarksvidda, North Norway. *Norges Geologiske Undersokelse Bulletin* **403**, 103–112.

Sinton, J. M. & Detrick, R. S. (1992). Mid-ocean ridge magma chambers. *Journal of Geophysical Research: Solid Earth* **97**, 197–216.

Skaar, J. A. A. (2014) 3D geophysical and geological modelling of the Karasjok Greenstone Belt. Department of Geoscience and Petroleum. NTNU: Norwegian University of Science and Technology.

Sobolev, A. V., Asafov, E. V., Gurenko, A. A., Arndt, N. T., Batanova, V. G., Portnyagin, M. V., Garbe-Schonberg, D. & Krasheninnikov, S. P. (2016). Komatiites reveal a hydrous Archaean deep-mantle reservoir. *Nature* **531**, 628–632.

Sparks, R. S. J. & Cashman, K. V. (2017). Dynamic magma systems: implications for forecasting volcanic activity. *Elements* **13**, 35–40.

Stokmo, E. B. (2020) Superimposed macro- and mesoscale folds, and their relation to ductile shear zones in the Karasjok Greenstone Belt, Finnmark, Norway. Department Of Geosciences. UiT: UiT The Arctic University of Norway.

Sun, S. S. & McDonough, W. F. (1989). Chemical and isotopic systematics of oceanic basalts: implications for mantle composition and processes. *Geological Society, London, Special Publications* **42**, 313–345.

Sun, S. S. & Nesbitt, R. W. (1978). Petrogenesis of Archaean ultrabasic and basic volcanics - evidence from rare-earth elements. *Contributions to Mineralogy and Petrology* **65**, 301–325.

Tarasewicz, J., White, R. S., Woods, A. W., Brandsdóttir, B. & Gudmundsson, M. T. (2012). Magma mobilization by downward-propagating decompression of the Eyjafjallajökull volcanic plumbing system. *Geophysical Research Letters* **39**.

Weaver, B. L. & Tarney, J. (1984). Empirical approach to estimating the composition of the continental crust. *Nature* **310**, 575–577.